

**Gradient of the Casimir force between Au surfaces of a sphere
and a plate measured using atomic force microscope in a
frequency shift technique**

C.-C. Chang,¹ A. A. Banishev,¹ R. Castillo-Garza,¹

G. L. Klimchitskaya,² V. M. Mostepanenko,³ and U. Mohideen¹

*¹Department of Physics and Astronomy,
University of California, Riverside, California 92521, USA*

*²North-West Open Technical University,
Polustrovsky Avenue 59, St.Petersburg, 195597, Russia*

*³Central Astronomical Observatory of the Russian Academy of Sciences,
Pulkovskoye chaussee 65/1, St.Petersburg, 196140, Russia*

Abstract

We present measurement results for the gradient of the Casimir force between an Au-coated sphere and an Au-coated plate obtained by means of an atomic force microscope operated in a frequency shift technique. This experiment was performed at a pressure of 3×10^{-8} Torr with hollow glass sphere of $41.3 \mu\text{m}$ radius. Special attention is paid to electrostatic calibrations including the problem of electrostatic patches. All calibration parameters are shown to be separation-independent after the corrections for mechanical drift are included. The gradient of the Casimir force was measured in two ways with applied compensating voltage to the plate and with different applied voltages and subsequent subtraction of electric forces. The obtained mean gradients are shown to be in mutual agreement and in agreement with previous experiments performed using a micromachined oscillator. The obtained data are compared with theoretical predictions of the Lifshitz theory including corrections beyond the proximity force approximation. An independent comparison with no fitting parameters demonstrated that the Drude model approach is excluded by the data at a 67% confidence level over the separation region from 235 to 420 nm. The theoretical approach using the generalized plasma-like model is shown to be consistent with the data over the entire measurement range. Corrections due to the nonlinearity of oscillator are calculated and the application region of the linear regime is determined. A conclusion is made that the results of several performed experiments call for a thorough analysis of the basics of the theory of dispersion forces.

PACS numbers: 78.20.-e, 12.20.Fv, 12.20.Ds

I. INTRODUCTION

Modern measurements of the Casimir force¹ have been actively pursued since 1997 (reviews^{2,3} contain the description of all experiments performed up to 2001 and 2009, respectively). In this period it has been conclusively demonstrated that the Casimir force can be reproducibly measured using modern laboratory techniques. The obtained results have found prospective applications ranging from nanotechnology⁴⁻⁶ to constraining parameters of fundamental physical theories beyond the standard model.⁷⁻¹²

The Lifshitz theory^{13,14} of the van der Waals and Casimir forces has been applied to two semispaces made of real materials at nonzero temperature¹⁵⁻¹⁷ and generalized for interacting surfaces of arbitrary shape.¹⁸⁻²⁰ The comparison between the measurement data and computations using the Lifshitz theory with particular dielectric permittivities has shown areas of disagreement. It was found that theoretical predictions obtained using the dielectric permittivity of the Drude model are excluded by the data of three precise experiments²¹⁻²⁴ on indirect dynamic determination of the Casimir pressure between two parallel metallic plates performed in the configuration of a sphere above a plate by means of a micromachined oscillator at separations from 0.16 to 0.75 μm (note that in the modern phase of measurements of the Casimir force the experimental configuration of two parallel plates was used only in Ref.²⁵). The same data were found consistent with the Lifshitz theory combined with the generalized plasma-like model.²⁴ Coincidentally it was proven^{3,26} that the Lifshitz theory combined with the plasma model satisfies the third law of thermodynamics (the Nernst heat theorem), but violates this fundamental physical principle when the dielectric permittivity of the Drude model for metals with perfect crystal lattices is used. Keeping in mind that the dielectric response of metals for real electromagnetic fields is correctly described by the Drude model, whereas the plasma model is an approximation applicable only at sufficiently high frequencies, these results initiated continuing discussions.^{2,27-29} Specifically, it was suggested to carefully check all approximations used in the computations, in particular, the proximity force approximation (PFA), reconsider the role of such background effects as electrostatic patch potentials and surface roughness, and to determine the role of variations in optical data of the Au films.

Results similar in spirit were obtained with dielectric surfaces. Thus, measurements of the difference in the Casimir forces between an Au-coated sphere and Si plate in the

presence and in the absence of a laser pulse on a plate measured by means of an atomic force microscope (AFM) at short separations were found to be consistent with the Lifshitz theory when neglecting the dc conductivity of dielectric Si in the dark phase.^{30,31} The same measurement data exclude the Lifshitz theory with the dc conductivity of Si taken into account in the absence of a laser pulse.^{30,31} Measurements of the thermal Casimir-Polder force between ^{87}Rb atoms belonging to the Bose-Einstein condensate and SiO_2 plate³² agree well with the Lifshitz theory neglecting the dc conductivity of SiO_2 , but were found³³ in clear disagreement with the same theory including the dc conductivity in the computations. On the theoretical side, it was demonstrated³⁴ that the Lifshitz theory for dielectrics with included dc conductivity violates the Nernst heat theorem. Theoretical and experimental advances in the Casimir effect, including the unresolved problems, are discussed in the book,³⁵ whereas reviews^{36,37} present details of experiments with fluids and semiconductors, respectively.

Recently two more experiments were performed. The first of them³⁸ was performed by means of a torsion pendulum. It reports observation of the thermal Casimir force at large separations $0.7 - 7.3 \mu\text{m}$ between a spherical lens of $R = 15.6 \text{ cm}$ radius of curvature and a plane plate both coated with Au, as predicted by the Lifshitz theory using the Drude model. This experiment did not directly measure the Casimir force but up to an order of magnitude larger total force presumably determined by large electrostatic patches.³⁸ The Casimir force was extracted using a fitting procedure with two fitting parameters. The results of this experiment are in contradiction with two earlier torsion-pendulum experiments performed at large separations,^{39,40} and with dynamic measurements by means of micromachined oscillator.²¹⁻²⁴ These results have been called into question in the literature.^{41,42} The second of two recent experiments measured the Casimir force between an Au-coated sphere and an indium tin oxide (ITO) plate using an AFM in the static mode.^{43,44} It was shown that the UV treatment of an ITO plate results in up to 35% decrease in the magnitude of the Casimir force. On the basis of the Lifshitz theory this was explained by the Mott-Anderson phase transition of the ITO plate under the influence of UV treatment from metal to dielectric state, where the dc conductivity of ITO was omitted in computations. However, the inclusion of the dc conductivity of the UV-treated sample results in the contradiction of theoretical predictions with the experimental data.

Keeping in mind that the Lifshitz theory faces outstanding problems when using the

most natural and well tested models of dielectric response, it is important to perform more experiments on measuring the Casimir force between Au surfaces particularly using a laboratory setup different in technique and preparation of the test bodies and from those applied previously. In this paper we report measurements of the gradient of the Casimir force between an Au-coated hollow glass microsphere and an Au-coated sapphire plate by means of the dynamic AFM operated in the frequency shift technique (also referred to as frequency modulation). Previously measurements of the Casimir interaction between Au surfaces, allowing discrimination between predictions of the Drude and plasma models at short separations, were performed by means of a micromachined oscillator.²¹⁻²⁴ The experiment⁴⁵ with Au-coated surfaces of a sapphire disk and a polystyrene sphere using the static AFM was not enough precise to discriminate between different theoretical predictions. Similar AFM experiments have been performed in the dynamic mode using the phase shift^{46,47} and the amplitude shift⁴⁸ techniques. These have also not been precise enough to distinguish between the various models. In the frequency shift technique, the gradient of the Casimir force acting on the cantilever modifies the resonant frequency and the corresponding shift in frequency is recorded using a phase locked loop (with application to AFM the frequency shift technique is discussed in detail in Ref.⁴⁹). As a result, the frequency shift technique is free from limitations inherent to the phase shift and amplitude shift techniques and leads to a factor of 10 larger sensitivity. This allows discrimination between different theoretical approaches to the thermal Casimir force using the AFM.

This experiment was performed at a lower pressure of 3×10^{-8} Torr. Much attention was paid to electrostatic calibration. Specifically, all mechanical drifts were measured and the corresponding corrections in the measured quantities were introduced. As a result, the residual potential difference, the closest sphere-plate separation and the coefficient converting the frequency shift into the force gradient were found independent of separation distance. The numerical simulation of the electrostatic force due to electrostatic patch potentials was performed. It was shown that for both small and large patches the residual potential between the sphere and the plate would heavily depend on the separation for patch sizes of order or larger than this separation. The absence of such dependence in our measurements confirms the fact that the interacting regions of the test bodies used were free from work function inhomogeneities of a size scale which may significantly distort the total force measured.

The gradient of the Casimir force between the sphere and the plate was obtained in two

different ways: from the total force (electric plus Casimir) with different applied voltages and electric force subtracted (44 measurement sets) and in an immediate way by the application of only the compensating voltage to counterbalance the residual potential difference (40 measurement sets). The mean gradients of the Casimir force obtained in these two ways were found in good mutual agreement and in agreement with the measurements by means of the micromachined oscillator.^{23,24} The random, systematic and total experimental errors at a 67% confidence level have been determined.

The experimental data were compared with theoretical predictions of the Lifshitz theory. In so doing the corrections to the PFA obtained from exact calculations in the sphere-plate geometry were taken into account. Computations of the gradient of the Casimir force were performed taking the surface roughness into account. The roughness profiles were investigated using an atomic force microscope. In computations the optical data for the complex index of refraction of Au from different sources have been used. The theoretical prediction using the Drude model approach (i.e., the tabulated optical data for the imaginary part of dielectric permittivity extrapolated to lower frequencies by the imaginary part of the Drude model) is excluded by the results of our measurements at a 67% confidence level over the separation region from 235 to 420 nm. The Lifshitz theory combined with the generalized plasma-like model is shown to be consistent with the measurement data over the entire measurement range from 235 to 750 nm. We have also studied the oscillator system used in the experiment in the nonlinear regime and determined the application region of the linear equation used to convert the frequency shift of the oscillator into the gradient of the Casimir force.

The structure of the paper is as follows. In Sec. II we describe the experimental setup and scheme for dynamic measurements of the gradient of the Casimir force in the frequency shift technique. Electrostatic calibrations and related problems are considered in Sec. III. Here, we pay special attention to the problem of patch potentials by performing numerical simulations of additional forces due to electrostatic patches or contaminants. All calibrations are performed with account of the mechanical drift in separation distances. Section IV contains measurement results for the gradient of the Casimir force. We present the measurement data obtained in two ways, with applied compensating voltage and with applied different voltages with subsequent subtraction of the electric force. In Sec. V we perform the comparison between experiment and theory. The role of nonlinear effects in dynamic

measurements using an AFM is discussed in Sec. VI. In Sec. VII the reader will find our conclusions and discussion.

II. SETUP AND SCHEME FOR DYNAMIC MEASUREMENTS IN THE FREQUENCY SHIFT TECHNIQUE

The main role in the setup for dynamic measurement of the gradient of the Casimir force in the frequency shift technique [see Fig. 1(a)] is played by the detection system. This system consists of an AFM cantilever with attached sphere, piezoelectric actuator, fiber interferometers, light source and phase locked loop (PLL). The detection system was placed in a high vacuum chamber [see Fig. 1(a)]. The high vacuum down to 10^{-9} Torr was created and sustained with the help of different pumps, valves, gauges and various vacuum feed-throughs. We begin the description of the setup with the vacuum system.

For the main vacuum chamber an 8" six-way stainless steel cross was used. This chamber was mounted on a 8" ion pump. The chamber was first evacuated by a turbo-pump backed by an oil-free dry scroll mechanical pump. The first two pumps can achieve a vacuum down to 2×10^{-7} Torr. The ion pump allows to reach a vacuum of 10^{-9} Torr. The vacuum chamber was separated from the turbo and mechanical pumps by a gate valve which can be closed when only the ion pump is to be used. The low vacuum pressure less than 10^{-3} Torr was measured with a thermal-conductivity gauge. For measuring high vacuums of 10^{-9} Torr an ionization gauge was used. The main vacuum chamber was supported on a damped optical table having a large mass to reduce the mechanical noise. For the electrical connections to elements inside the vacuum chamber D-type subminiature connections were used offering UHV feed-through with 25 pins which were hermetically sealed and insulated by means of glass ceramic bonding. For optical connections a home-built optical fiber feed-through was used made on a CF flange welded with a clean stainless tube. A cladding-stripped 1550 nm fiber was inserted through the steel tube and sealed using Varian vacuum Torr seal.

We continue the description of the setup by acquaintance with the fiber interferometers [see Fig. 1(b) for more details]. Two fiber optic interferometers were used. One interferometer monitored the cantilever oscillation. The second recorded the displacement of the Au plate mounted on the AFM piezoelectric actuator. For constructing the interferometer, we used a 1550 nm single mode fiber which has extremely low bending loss and low splice

loss compared to the standard SMF-28 1550 nm fiber. A super luminescent diode with a wavelength of 1550 nm, served as the light source for the cantilever frequency measurement interferometer. The coherence length of the diode was $66 \mu\text{m}$. A short coherence length is necessary to avoid noise from spurious interferences from unwanted reflections. An optical isolator with FC-APC connectors joined the diode to a 50/50 directional coupler. We used the typical fused-tapered bi-conic coupler at 1550 nm wavelength with return-loss of -55dB relative to the input power. To reduce the signal power attenuation, we avoided bulkhead connectors which usually have $\sim 0.3\text{dB}$ power loss. A fiber coupled laser source with a wavelength of 635 nm was used for the Au plate displacement interferometer. In our experimental setup, we used a commercial anodized black xyz-stage [see Fig. 1(b)] to move the fiber end vertically above and close to the cantilever. But the anodizing may significantly increase outgassing rates because of its porous structure. Therefore special treatments were done before placing the xyz-stage into the high vacuum chamber. The xyz-stage was first disassembled and the parts scrubbed with strong solution of detergent in an ultrasonic cleaner. They were then rinsed with very hot water. Next they were immersed in a 10% solution of sodium hydroxide (NaOH) saturated with common salt (NaCl) at 80°C . The parts were then polished in a conventional wheel polishing machine. They were then immersed in 10% solution of hydrochloric acid to obtain a bright finish. This was then followed by rinsing in DI water and reassembly of the xyz stage using powder-free disposable plastic gloves. Finally the xyz stage was rinsed with acetone followed by ethyl alcohol before insertion into the vacuum chamber.

The interferometer system [see Fig. 1(b)] used for measuring the frequency shift consists of the following parts. The output of the directional couplers was measured with InGaAs photodetectors. A low noise photodetector and amplifier system was fabricated for the cantilever interferometer. To avoid any potential errors or noise from the divider or balancing system, the InGaAs diode was coupled to an OPA627 low noise operational amplifier (very high input impedance $\sim 10^{13}\Omega$) as a trans-impedance amplifier. The output of the interference signal was fed into a band-pass filter cascaded by low and high pass filter to cut off unwanted frequency bands. The high-pass filter helped us to remove the noise in the excitation signal from frequency modulation controller and the low-pass filter removed $1/f$ and environmental noise. For frequency demodulation we use a PLL (Nano Surf.). The PLL frequency demodulator system combines a controller module and detector module to

measure the force gradient induced resonant frequency shift. The output of the high pass filter was fed to the PLL for the frequency demodulation. The output of the PLL was connected to a piezoelectric transducer which drives the cantilever at its resonant frequency $\omega = 2\pi \times 1.604$ kHz with a constant amplitude. The oscillation amplitude of the cantilever was fixed at < 10 nm for all separations. The output of the low pass filter was used to form a closed loop proportional-integral-derivative (PID) controller and to maintain constant separation distance between the fiber end and the cantilever during the frequency modulation detection. The distance was kept constant using a piezoelectric actuator with the PID controller.

Now let us consider the detection system. As mentioned above, the force gradient was measured between an Au-coated plate and Au-coated sphere attached to the cantilever [see Fig. 1(b)]. In difference with previous experiments, to achieve high resonance frequencies (and therefore low noise) hollow glass microspheres and stiffer rectangular Si cantilevers were used. The Si cantilevers are conductive, which is necessary for electrical contact to the sphere. The surfaces of the hollow glass spheres are smooth as they are made from liquid phase. We followed a special procedure for cleaning the spheres before attachment to the cantilever. The sphere cleaning procedure removes organic contaminants and debris from the surface. The first step in the cleaning process was to make a 10 ml solution of ethanol into which the spheres were deposited. This solution was thoroughly mixed in a vortex mixer for about 1 minute. Then, using a pipette, the alcohol was extracted from the solution, leaving the spheres in the vial. To remove strongly attached adsorbates and debris, a 10 ml solution of Hydrogen peroxide (H_2O_2) was added to the vial. A vortex mixer was again used to mix for about 2 min. The O_2 gas released from the solution removed any attached debris from the spheres. Next, the H_2O_2 was extracted with a pipette, and the spheres were immersed in 10 ml of ethanol again. To completely separate the debris from the spheres, we centrifuged the alcohol/sphere solution, for 10 minutes. The large radius, clean hollow spheres float to the top of the mixture and the debris sediment to the bottom. We used a pipette to remove the spheres at the top and place them in a pyrex petri dish to dry. The dried spheres were then mounted on the conductive Si cantilevers using Ag epoxy. The cantilever-sphere system and a 10 mm in diameter sapphire disk were coated with Au in an oil-free thermal evaporator described elsewhere.⁵⁰ The sphere cantilever system was rotated to get a uniform coating. In contrast to previous experiments only the tip of the

cantilever with the sphere was coated with Au. Complete coating of the cantilever leads to large decrease in its oscillation Q-factor and loss of sensitivity. The thickness of the Au coating was measured to be 280 ± 1 nm using an AFM. The radius of the sphere was measured to be $R = 41.3 \pm 0.2$ μm using a scanning electron microscope. Thus, the sphere coating was thicker and the sphere radius smaller than in the static AFM experiment.⁴⁵

The cantilever with the sphere was placed in a specially fabricated holder [see Fig. 1(b)] containing two piezos (first connected to the PID loop and the second to the PLL). The Au plate was mounted on top of a tube piezoelectric actuator from a commercial AFM capable of traveling a distance of 2.3 μm . Ohmic contacts were made to the Au plate through a $1\text{ k}\Omega$ resistor. To minimize electrical ground loops all the electrical ground connections were unified to the AFM ground. The calibration of the tube piezoelectric actuator was done using the second interferometer and is described in previous work.⁵¹ To change the sphere plate distance using the piezoelectric actuator and avoid piezo drift and creep, a continuous 0.01 Hz triangular voltage signal was applied to the actuator. The chamber was evacuated using the turbo pump [see Fig. 1(a)] to a pressure of 2×10^{-7} Torr. Next, the ion pump [see Fig. 1(a)] was turned on and the turbo pump was isolated from the chamber by closing the $6''$ gate valve. When chamber reaches 3×10^{-8} Torr pressure, the experiment was started.

The measurement scheme allowing determination of the gradient of the Casimir force is the following. In a dynamic experiment using the frequency shift technique the total force gradient acting on the cantilever due to interaction of the sphere and plate surfaces modifies the natural resonance frequency of the oscillator. The corresponding change in the frequency $\Delta\omega = \omega_r - \omega_0$, where ω_r is the resonance frequency in the presence of external force $F_{\text{tot}}(a)$, a is the separation between the sphere and the plate, is recorded by the PLL. The total force $F_{\text{tot}}(a)$ is the sum of the electrostatic force $F_{\text{el}}(a)$ and the Casimir force $F(a)$

$$F_{\text{tot}}(a) = F_{\text{el}}(a) + F(a). \quad (1)$$

Note that even if no voltage is applied to the Au plate and the Au sphere is grounded, there is some residual potential difference V_0 between the interacting bodies. This is caused by different connections or work functions of sphere and plate materials from patches and adsorbates on their surfaces. To perform the electrostatic calibrations of our measurement system, the Au coated plate was connected to a voltage supply operating with 1 μV resolution. Then 11 different voltages V_i in the range from -87.4 to 32.6 mV were applied to the

Au plate, while the sphere remained grounded.

Starting at the maximum separation, the plate was moved towards the sphere and the corresponding frequency shift was recorded at every 0.14 nm. As was mentioned above, the sphere-plate force acting on the cantilever causes a change in the resonance frequency. In the linear regime it is given by

$$\Delta\omega = -\frac{\omega_0}{2k} \frac{\partial F_{\text{tot}}(a)}{\partial a}, \quad (2)$$

where k is the spring constant of the cantilever. Equation (2) is an approximate one. In Sec. VI it is obtained from the solution of a more complicated nonlinear problem and the application region of this equation is determined. The electric force entering Eq. (1) is expressed as

$$F_{\text{el}}(a) = X(a, R)(V_i - V_0)^2, \quad (3)$$

where the function $X(a, R)$ can be written in the form^{35,52}

$$X(a, R) = 2\pi\epsilon_0 \sum_{n=1}^{\infty} \frac{\coth \alpha - n \coth n\alpha}{\sinh n\alpha},$$

$$\cosh \alpha = 1 + \frac{a}{R} \quad (4)$$

and ϵ_0 is the permittivity of the free space. For convenience in computations this function can be presented approximately^{35,53} as the sum of powers $c_i(a/R)^i$ from $i = -1$ to $i = 6$. The absolute separation a is measured between the zero levels of the roughness on the surfaces of a sphere and a plate (see Sec. V). Experimentally the absolute separation is found as $a = z_{\text{piezo}} + z_0$, where z_{piezo} is the plate movement due to the piezoelectric actuator and z_0 is the point of closest approach between the Au sphere and Au plate (note that in this experiment the separation at the closest approach is much larger than the separation on contact of the two surfaces).

Substituting Eq. (1) in Eq. (2) and using Eq. (3), one obtains

$$\Delta\omega = -\beta(V_i - V_0)^2 - C \frac{\partial F}{\partial a}, \quad (5)$$

where $C \equiv C(k, \omega_0) = \omega_0/(2k)$ and $\beta \equiv \beta(a, z_0, C, R) = C \partial X(a, R)/\partial a$. Here, the first term on the right-hand side is associated with the gradient of electrostatic force caused by a constant voltage applied to the plate while the sphere remained grounded. The second term is proportional to the gradient of the Casimir force. Below Eq. (5) is used for the

determination of the gradients of the Casimir force from the measured data for the frequency shifts.

III. ELECTROSTATIC CALIBRATIONS AND RELATED PROBLEMS

To determine the gradients of the Casimir force from Eq. (5) one needs to know the precise values of the involved parameters β , C and z_0 . These can be determined by applying different voltages V_i to the plate and investigating the parabolic dependence of the frequency shift expressed in arbitrary units on V_i . The calibration procedure requires much care because errors in calibration parameters due, for instance, mechanical drift result in respective errors in the measured Casimir force or its gradient. Electrostatic calibrations in measurements of the Casimir force have created much discussion in the literature.^{54–58} Specifically, in some cases it was observed⁵⁴ that the residual potential difference V_0 depends on separation: $V_0 = V_0(a)$. This was attributed to the probable role of the patch potentials arising due to the polycrystal structure of metallic coatings⁵⁹ or dust and contaminants on the surfaces⁶⁰ (for a pure Coulombian interaction, similar to the applied voltages considered above, V_0 is separation-independent). It was even speculated⁵⁸ that patches may render the experimental data^{23,24} at distances below $1\ \mu\text{m}$ compatible with theoretical predictions based on the Drude model. Below we present the results of numerical simulation of the electrostatic force due to patch potentials and then describe the electrostatic calibrations.

A. Numerical simulations of additional forces due to electrostatic patches

Here, we consider the force arising from a spatial distribution of electrostatic potentials on the surface of an Au plate in close proximity to an Au sphere for typical parameters of experimental interest. A realistic variation of the patch potentials was chosen in the range between -90 and $90\ \text{mV}$. This was based on the maximum difference in the workfunctions between the $\langle 100 \rangle$ and the $\langle 111 \rangle$ crystal orientations of Au.⁶¹ The electrostatic force between the Au plate with patches and the grounded Au sphere was numerically simulated using 3-dimensional finite element analysis commercial software package (COMSOL Multiphysics).

For this purpose an additional package of the AC/DC module of COMSOL Multiphysics, which is software specifically designed for problems with electrodynamics and electrostatics,

was used. The physical system used in the simulation was drawn with the CAD module of COMSOL Multiphysics and the boundary conditions discussed below were assigned.

We first drew a $100\ \mu\text{m}$ diameter sphere and $120 \times 120 \times 20\ \mu\text{m}^3$ plate (see Fig. 2). The sphere and plate were placed inside a rectangular box held at constant potential. To represent the patches, square grids of various sizes were made on the plate. The size of the grids varied between $300\ \text{nm}$ to $6000\ \text{nm}$. Random potentials between -90 to $+90\ \text{mV}$ were assigned to the patches using a random number generator. There was no height difference between the patches and the surrounding.

After that, the governing equation, that needs to be solved, with the given boundary conditions was defined. For the electrostatic force between two metallic objects in vacuum with applied voltages to the plate, the governing equation is the Poisson equation: $\nabla \varepsilon_0 \varepsilon_r \nabla V = 0$, where ε_r is the relative permittivity set equal to unity and V is the potential. The numerical program solves the electric field and potential at each coordinate in the 3-dimensional space. It finds the force for a given configuration of potentials on the surfaces. The force acting on the sphere was obtained by integrating the Maxwell stress tensor along the sphere boundary.

The boundary conditions were as follows. The sphere, and the external box were grounded (potentials were set equal to zero). The sphere and plate were positioned at some distance a . First the force only due to the patches, F_{pat} , was calculated. Here the potential applied to the plate is kept at zero and only the patches have nonzero potentials. Next, the sphere-plate force for various potentials V applied to the plate, F_V , was calculated, when the patch potentials were set to zero. The value of the applied potential V to the plate was varied till $F_V = F_{\text{pat}}$. This value of V is equal to V_0 , the potential that is necessary to compensate the electrostatic force from the patches. Zero electrostatic sphere-plate force was confirmed for the plate with patches by applying a potential of V_0 to the plate.

To achieve the highest resolution in solving the electrostatic problem we used the following parameters for generation of the surface mesh: 1) The maximum element size is 10^{-7} ; 2) Maximum element size scaling factor is 1; 3) Element growth rate is 1.2; 4) Mesh curvature factor is 0.2; 5) Mesh curvature cutoff is 0.001; 6) Resolution of narrow regions is 1. The latter parameter was used to control the number of elements generated in a narrow region. Among these parameters, 3)–6) are very important if a finer mesh is required, especially for complicated objects with sharp, narrow edges or small holes.

Now we consider the results of the influence of the random distribution of electrostatic

patch potentials on the electrostatic force between the gold sphere and plate. The investigations were performed for periodic patches with random electrostatic potentials distribution for different sphere-plate separations. The corresponding compensation voltage V_0 when $F_V = F_{\text{pat}}$ was found at every separation.

In the finite element analysis method the errors mainly result from the discretization of the surface mesh elements. To obtain the necessary precision and optimize the computation time, the number of mesh elements was restricted to 243122. To calibrate the simulation, the theoretical force was compared to that obtained from the numerical simulation. In these checks a uniform plate with no patches was used. The sphere and plate were placed at 100 nm separation. The voltage V was applied to the plate and the corresponding F_V was found using the numerical simulation. The value was found to be precise to within 0.23% of the theoretical value. This was repeated for several sphere-plate separation distances between 50–1000 nm.

First the role of large patches was studied. Patch sizes of $6 \times 6 \mu\text{m}^2$ were used on the plate. The distance between the patches was kept at $6 \mu\text{m}$. The residual potentials that will compensate the electrostatic force of the patches were found for sphere-plate separation distances from 50 nm to 1000 nm. These are shown in Fig. 3(a) as solid squares. The residual potential was found to change as a function of the separation distance. The change decreases with separation and is very small at 1000 nm even for these $6 \mu\text{m}$ patches. Next the separation distance between the patches was increased to $9 \mu\text{m}$, while the patch size remained fixed. The calculations were repeated as before for different sphere-plate separation distances and results are shown as solid circles in Fig. 3(a). The same exercise was repeated for $12 \mu\text{m}$ distance between the patches and the compensation voltage found is shown as solid triangles in the same figure. It is clear from the figure that while the values of the compensation potential are different for different separation distances the dependence of V_0 on separation is very similar. This shows that even for these relatively large patches it is possible to obtain a region of separation distance on the order of a micron where the compensation potential is relatively independent of separation distance.

Next we investigated the role of smaller patches of size $900 \times 900 \text{ nm}^2$. The distances between the patches were fixed at 600 nm. The simulation was repeated and the compensation voltage was found for separation distances between 50 nm and 1000 nm. The values are shown as solid triangles in Fig. 3(b). The V_0 is found to vary as a function of the separation

distance from 9 mV to 21 mV. Then the patch size was decreased to $600 \times 600 \text{ nm}^2$ while the patch-patch distance remained fixed. The simulations were repeated and the compensation voltage as a function of separation is shown as solid circles in Fig. 3(b). The smaller patches are seen to lead to smaller V_0 which also varies less with separation distance. The variation seems to be correlated with the patch size and the V_0 varies little for separation distances greater than the patch size.

Then the patch size was further reduced to $300 \times 300 \text{ nm}^2$ and simulations repeated for the same patch-patch distance. For these smaller patches the plate size was reduced to $32 \times 32 \mu\text{m}^2$ to optimize the computation time. The results of the compensation voltages are represented by solid squares in Fig. 3(b). It is clear that the compensation voltage V_0 of the smaller patches have a correspondingly weak dependence on the separation distance. It is worth noting that the $300 \times 300 \text{ nm}^2$ patches have a V_0 which is almost independent of the separation distance particularly above 300 nm. It should be mentioned that the crystallite sizes observed on the Au coated plates used in experiments are even less than 300 nm. This implies that clean samples where the patch effects originate only from crystallite size should show a V_0 that is independent of sphere-plate separation distance. It should also be emphasized that the values of V_0 between 8 and 9 mV computed are similar to those observed in experiments. This lends credence to the notion that the patches present in experiments are of similar size and potential as has been simulated.

At the same time, patches or surface contaminants of about $2 \mu\text{m}$ size, like those considered recently⁵⁸ in order to make the experimental data^{23,24} compatible with theoretical predictions of the Lifshitz theory combined with the Drude model, lead to a very strong dependence of V_0 on the separation distance at separations up to a few hundred nanometers [see the upper line marked by solid triangles in Fig. 3(b)]. In several experiments^{21-24,38,43-45,55} it was experimentally found, however, that $V_0 = \text{const}$ over the entire measurement range. This rules out the hypothesis⁵⁸ that the deviation between the experimental data^{23,24} and the Drude model predictions may be attributed to the role of large patches. We will return to this point in the next section in connection with our measurements.

B. Calibration with account of mechanical drift

Now we describe how the parameters of our measurements, V_0 , z_0 and C were determined by means of electrostatic calibrations. We begin with the determination of V_0 . From Eq. (5) it can be seen that the frequency shift $\Delta\omega$ has a parabolic dependence on the voltage V_i applied to the plate and reaches a maximum at $V_i = V_0$. Thus, V_0 can be extracted from this dependence using χ^2 -fitting procedure. The curvature of the parabolas is related to β and includes the closest separation and the cantilever parameter C . Thus, these parameters can be also extracted from the fit. In order to test for systematic errors in the fitting parameters, the fitting procedure was repeated many times at different distance ranges.

In the first step, 11 different voltages V_i were applied to the plate and the corresponding frequency shift signal due to the total force gradient was measured. Then, we subtracted any drift of the frequency shift signal. For this purpose we used the fact that for separations larger than $2\ \mu\text{m}$ the total force between the sphere and plate is below the instrumental sensitivity. At these separations, the noise is far greater than the signal and in the absence of systematic errors the signal should average to zero. Then the correction due to the drift in sphere-plate separation can be measured. The effect of the drift can be observed in Fig. 4(a), where 8 repeated measurements of the frequency shift signal $S_{\Delta\omega}$ as a function of the sphere-plate separation change Δz are shown for same applied voltage to the plate. Drift causes the separation to increase by around 1 nm in 700 s, where 100 s correspond to the time taken to make the one measurement [note that positional precision much better than 1 nm is achieved in this experiment as observed in Fig. 4(a)]. To calculate the drift rate, the change in position at one frequency shift signal is plotted as a function of time as shown in Fig. 4(b). This was repeated for 15 different signals and the average drift rate was found to be 0.002 nm/s. The separation distances in all measurements and between subsequent measurements were corrected for this drift rate.

After applying the drift correction the residual potential V_0 between the sphere and plate was found. The frequency shift signals at every 1 nm separation were found by interpolation (data acquisition was done every 0.14 nm). From the parabolic dependence of the electric force gradient shown in Eq. (5), V_0 can be identified at the position of the parabola maxima. The frequency shift signal was plotted as a function of the applied voltages V_i at every separation and the corresponding V_0 and curvature of the parabola β were found. This V_0

is shown in Fig. 5(a) as a function of separation distance with a step of 1 nm. In Fig. 5(b) we show the systematic errors of each individual V_0 , as determined from the fit. The mean systematic error equal to 0.86 mV is shown by the horizontal line. The random error in the mean V_0 averaged over all separations is equal to 0.04 mV. This finally leads to a mean $V_0 = -27.4 \pm 0.9$ mV where the total error of 0.9 mV is determined at a 67% confidence level. As can be seen from Fig. 5(a), the mean V_0 is independent of separation over the entire measurement range. To check this observation, we have performed the best fit of V_0 to the straight line [see Fig. 5(a)] leaving its slope as a free parameter. It was found that the slope is 0.000012 ± 0.000255 mV/nm, i.e., the independence of V_0 on separation was confirmed. Note that the larger spread of the individual V_0 at larger separations is caused by the smaller values of the total force measured. This, however, does not influence the systematic errors in the determination of V_0 from the fit [see Fig. 5(b)]. The total error in the mean value of V_0 does not influence the systematic error in the measurement scheme with fixed V_0 which is mostly determined by instrumental noise (see Sec. IVA).

The observed independence of V_0 on a should be considered in connection with the problem of patch potentials discussed in Sec. IIIa. According to our discussion, the patches due to different crystal orientations of the polycrystal sample, surface contaminants and dust may lead to different dependences of V_0 on a . Specifically, our simulations show that V_0 depends only slightly on a for patch sizes smaller than the separation distance. This is the case of patches due to different crystal orientations. The influence of this type of patches is automatically taken into account in our measurements either in the value of subtracted electric force or in the value of applied compensating voltage (see Sec. IV). From our simulations it also follows that V_0 depends heavily on a for patch sizes of order or larger than the separation distance. According to Fig. 4, in our experiment V_0 remains constant up to $a = 750$ nm. Thus, the existence on our plate of patches of more than 2000 nm size discussed in the literature⁵⁸ is incompatible with our measurement data for V_0 . As was mentioned in the introductory part of Sec. III, the dependence of V_0 on separation was observed in different experiments on the Casimir force (see, e.g., Refs.^{46–48,54,56,62}). It might be caused for different reasons including the mechanical drift considered above. In each case the specific reason can be only determined from a complete analysis of the setup and all the details of that particular experiment.

The next step was to determine the separation distance at closest approach z_0 and the

coefficient C in Eq. (5). As was explained above, these parameters can be found from the dependence of the parabola curvature β on distance a . The corresponding theoretical expression for parabola curvature was fit to the measured data for β as function of the separation distance. A least χ^2 -procedure was used in the fitting and the best values of z_0 and C were obtained. The fitting procedure was repeated by keeping the start point fixed at the closest separation, while the end point z_{end} measured from the closest separation was varied from 750 nm to 50 nm. In Fig. 6(a) the z_0 so determined is shown as a function of the end point used in the fit. The systematic errors in the determination of z_0 from the fit vary between 0.36 nm and 0.48 nm. In plotting Fig. 6(a) we have included the correction to the mechanical drift of separations, as described above. The values of z_0 are seen to be independent on z_{end} indicating the absence of errors resulting from z_{piezo} calibration. Similarly the value of the coefficient C was also extracted by fitting the β -curve as a function of separation to theoretical expression. The results obtained after the inclusion of the correction due to mechanical drift are shown in Fig. 6(b). Here, the systematic errors vary between 0.13 kHz m/N and 0.19 kHz m/N. The independence on z_{end} again indicates the absence of errors resulting from z_{piezo} calibration. The mean values of the calibration parameters obtained are $z_0 = 195.9 \pm 0.4$ nm and $C = 68.3 \pm 0.16$ kHz m/N. The indicated total errors are mostly determined by the systematic errors in the fit. These allow determination of absolute separation between the sphere and the plate and conversion of the frequency shift signal to the gradient of the total force.

IV. MEASUREMENT RESULTS FOR THE GRADIENT OF THE CASIMIR FORCE

In this section we present the data obtained for the gradient of the Casimir force as a function of separation and determine the random, systematic and total experimental errors. The data for the gradient of the Casimir force are obtained in two ways: with applied compensating voltage and with different applied voltages with subsequent subtraction of the gradient of electric force. The obtained results are compared with the measured in an earlier experiment.^{23,24}

A. Measurement scheme with applied compensating voltage

To compensate the residual potential difference between the sphere and the plate one should apply to the plate the potential $V_i = V_0$. Then the electric force vanishes and from Eq. (5) we obtain the gradient of the Casimir force

$$F'(a) = \frac{\partial F(a)}{\partial a} = -\frac{1}{C}\Delta\omega. \quad (6)$$

The dependence of the Casimir force gradient on separation was measured 40 times. The mean values of the force gradient with a step of one nanometer are shown as black dots in Fig. 7 and over a more narrow separation region in the inset to Fig. 7. In the same figure all 40 individual measured values of the Casimir force gradient are shown as grey dots with a step of 5 nm (in the inset a step size of 1 nm is shown).

The statistical properties of the experimental data measured are characterized by the histograms presented in Figs. 8(a) for $a = 235$ nm and 8(b) for $a = 275$ nm. The histograms are described by Gaussian distributions with the standard deviations equal to $\sigma_{F'} = 0.89 \mu\text{N}/\text{m}$ [Fig. 8(a)] and $\sigma_{F'} = 0.87 \mu\text{N}/\text{m}$ [Fig. 8(b)]. The values of the respective mean gradients of the Casimir force are $F' = 73.58 \mu\text{N}/\text{m}$ [Fig. 8(a)] and $F' = 41.07 \mu\text{N}/\text{m}$ [Fig. 8(b)]. The solid and dashed vertical lines are the theoretical predictions from the plasma and Drude model approaches, respectively (see Sec. V for a discussion).

Now we discuss the results of the error analysis. The random error in the gradient of the Casimir force calculated from 40 repetitions at a 67% confidence level is shown as the short-dashed line in Fig. 9 (note that all the experimental errors here and below are in fact determined with a step of 1 nm). The systematic error in the measured gradient is determined by the instrumental noise including the background noise level, and by the errors in calibration. In Fig. 9 the systematic error determined at a 67% confidence level is shown by the long-dashed line. The solid line in Fig. 9 demonstrates the total experimental error obtained by adding in quadrature the random and systematic errors. As can be seen in Fig. 9, all errors do not depend on separation, as it usually occurs³⁵ in measurements of the Casimir force by means of an AFM with applied compensating voltage at separations above 200 nm. The systematic error due to the instrumental noise is dominant and mostly determines the value of the total experimental error. The values of the mean measured force gradients at different separations (first column) together with the total experimental errors are shown in the second column of Table I. As can be seen from this table, the relative total

experimental error takes the minimum value of 0.69% at $a = 236$ nm, and then increases to 0.85%, 1.7%, 3.0%, 4.9%, and 11.6% at separations $a = 250, 300, 350, 400,$ and 500 nm, respectively. At $a = 746$ nm the relative total experimental error reaches a value of 47%.

It is of crucial importance to compare the gradients of the Casimir force measured here by means of the dynamic AFM with the results of a previous precision experiment^{23,24} performed by means of micromachined oscillator in Indianapolis University — Purdue University Indianapolis (IUPUI). In Fig. 10(a,b) the magnitudes of the mean Casimir pressure between two Au-coated plates determined in Refs.^{23,24} are shown by (a) black and (b) white lines over different separation regions. In accordance with the PFA, the magnitudes of the Casimir pressure measured here can be obtained from the force gradient as

$$|P(a)| = \frac{1}{2\pi R} F'(a). \quad (7)$$

In Fig. 10(a,b) the mean pressure magnitudes measured by us are shown as crosses. The arms of the crosses are determined by the absolute errors in the measurement of separations and force gradients (the latter are given in Fig. 9). Note that the error in separation distances determined at a 67% confidence level is approximately equal to the error in the point of the closest approach between the sphere and the plate, $\Delta a = \Delta z_0 = 0.4$ nm.

As can be seen in Fig. 10(a,b), the magnitudes of the mean Casimir pressures measured by us are in excellent agreement with the experimental results obtained previously.^{23,24} What's more in most of cases the centers of our experimental crosses are found in closest proximity to the magnitudes of mean experimental pressures measured in the IUPUI. To quantify this statement, in Table I (column 4) we present the gradients of the Casimir force which are obtained by multiplication of the pressure magnitudes $|P|$ measured in the experiment with micromachined oscillator^{23,24} by $2\pi R$, where R is the radius of our sphere. For convenience in comparison, the total experimental errors are indicated at the same 67% confidence level as in our measurements. From the comparison of columns 2 and 4 in Table I it can be seen that all differences between the respective gradients are in the limits of the total experimental errors in each experiment.

B. Measurement scheme with different applied voltages

Now we consider another experimental approach to measuring the gradients of the Casimir force in sphere-plate geometry, the same as was used to perform electrostatic calibrations. In this approach different voltages V_i are applied to the plate while the sphere remains grounded and the gradient of the total force (electrostatic plus Casimir) is measured. Then the gradient of the Casimir force is obtained from Eq. (5) as

$$F'(a) = -\frac{1}{C}\Delta\omega - \frac{\partial X(a, R)}{\partial a}(V_i - V_0)^2. \quad (8)$$

The dependence of the Casimir force gradient on separation was measured 4 times with 11 applied voltages leading to 44 force-distance curves. The mean values of the Casimir force gradient with a step of one nanometer are shown as black dots in Fig. 11(a) and over a more narrow separation region in the inset. All 44 individual values of the Casimir force gradient are shown as grey dots with the step of 5 nm (1 nm in an inset). It can be seen that Fig. 11(a) is very similar to Fig. 7 where the measured gradient of the Casimir force was obtained using another procedure.

The error analysis in this case is a little different than performed before. Specifically the random error calculated from 44 repetitions at a 67% confidence level is shown by the short-dashed line in Fig. 11(b). From the comparison with Fig. 9 it is seen that in the measurement scheme with different applied voltages the random error is slightly smaller. In addition to the two sources of systematic errors discussed in Sec. IVA, we now have one more systematic error in the gradient of electrostatic force subtracted in accordance to Eq. (8). As a result, the systematic error in the gradients of the Casimir force shown by the long-dashed line in Fig. 11(b) depends on separation. The total experimental error determined at a 67% confidence level is shown by the solid line in Fig. 11(b). At short separations the total error is slightly larger and at large separations slightly smaller than in the measurement scheme with applied compensating voltage. Specifically, at $a = 236$ nm it is equal to 0.75% and at $a = 500$ nm to 11.3%.

We present the values of mean gradients of the Casimir force measured with different applied voltages at different separations in column 3 of Table I together with their total experimental errors. From the comparison of column 3 with column 2 it can be seen that the gradients of the Casimir force measured with different applied voltages and with the compensating voltage are in very good mutual agreement. The differences between the

values in columns 2 and 3 calculated at any separation are significantly smaller than the total experimental errors indicated in Table I. This confirms the fact that our error analysis is conservative and the errors are overestimated giving high confidence to our conclusions with respect to the comparison with theory (see Sec. V). In a similar way, the comparison between columns 3 and 4 also demonstrates a very good agreement between our data and the results of IUPUI experiment^{23,24} within the limits much below allowed ones, as determined by the absolute errors.

V. COMPARISON BETWEEN EXPERIMENT AND THEORY

Now we compare the experimental data for the gradient of the Casimir force between the sphere and the plate with the predictions of the Lifshitz theory. In doing so we adapt the classical Lifshitz formula for two parallel plates to the sphere-plate geometry using the PFA and take into account recently calculated corrections to this approximate method.^{63,64} (The corrections computed previously^{65,66} cannot be used in this experiment because they are found for much larger values of a/R .) In the framework of the PFA, the Lifshitz-type formula for the gradient of the Casimir force between a sphere and a plate takes the form

$$F'_{\text{PFA}}(a, T) = 2k_B T R \sum_{l=0}^{\infty}{}' \int_0^{\infty} q_l k_{\perp} dk_{\perp} \sum_{\alpha} \frac{r_{\alpha}^2}{e^{2q_l a} - r_{\alpha}^2}. \quad (9)$$

Here, k_B is the Boltzmann constant and $T = 300$ K is the laboratory temperature (we restore this argument, omitted above, in theoretical equations). The quantity k_{\perp} is the projection of the wave vector on a plate, $q_l^2 = k_{\perp}^2 + \xi_l^2/c^2$, and $\xi_l = 2\pi k_B T l/\hbar$ with $l = 0, 1, 2, \dots$ are the Matsubara frequencies. The prime following the summation sign multiplies the term with $l = 0$ by 1/2 and $\alpha = \text{TM}, \text{TE}$ denotes the transverse magnetic and transverse electric polarizations of the electromagnetic field. The reflection coefficients r_{α} calculated along the imaginary frequency axis are given by

$$\begin{aligned} r_{\text{TM}} &\equiv r_{\text{TM}}(i\xi_l, k_{\perp}) = \frac{\varepsilon(i\xi_l)q_l - k_l}{\varepsilon(i\xi_l)q_l + k_l}, \\ r_{\text{TE}} &\equiv r_{\text{TE}}(i\xi_l, k_{\perp}) = \frac{q_l - k_l}{q_l + k_l}, \\ k_l &= \left[k_{\perp}^2 + \varepsilon(i\xi_l) \frac{\xi_l^2}{c^2} \right]^{1/2}, \end{aligned} \quad (10)$$

where $\varepsilon(i\xi_l)$ is the dielectric permittivity of boundary materials at the imaginary frequencies.

Computations of $F'(a, T)$ using Eq. (9) were performed with the two models of the dielectric permittivity of Au called in the literature the Drude model approach and the plasma model approach.^{3,35} In the Drude model approach, the tabulated optical data⁶⁷ for the imaginary part of dielectric permittivity of Au are used. They are extrapolated to lower frequencies by means of the imaginary part of the Drude model with the plasma frequency $\omega_p = 9.0$ eV and the relaxation parameter $\gamma = 0.035$ eV. Recently it was shown⁶⁸ that $\varepsilon(i\xi_l)$ obtained with this extrapolation is in excellent agreement with $\varepsilon(i\xi_l)$ obtained with the help of the weighted Kramers-Kronig relations from the measured tabulated data. In the plasma model approach, the same optical data with the contribution of free charge carriers subtracted are extrapolated to lower frequencies by means of the simple plasma model with the same value of the plasma frequency for Au.

The correction to the approximate expression (9) was recently calculated in the framework of the exact theory.^{63,64} The exact force gradient between the sphere of large radius and the plate was represented in the form

$$F'(a, T) = F'_{\text{PFA}}(a, T) \left[1 + \theta(a, T) \frac{a}{R} + o\left(\frac{a}{R}\right) \right], \quad (11)$$

where the quantity $\theta(a, T)$ was calculated. Specifically, for ideal metal bodies at $T = 0$ it was found^{63,64,69}

$$\theta(a, T) = \frac{1}{9} - \frac{20}{3\pi^2} = -0.564. \quad (12)$$

General expressions for $\theta(a, T)$ were also provided for real material bodies described by the frequency-dependent dielectric permittivity at nonzero temperature. In the framework of the Drude model approach, as described above, the quantity $\theta(a, T)$ was computed⁶⁴ as a function of separation at $T = 300$ K. It was found that $\theta(a, T)$ increases monotonically from -0.438 to -0.329 when a increases from 222 nm to 642 nm. This means that the error from using the PFA, which was taken equal to a/R in the analysis of previous experiments^{21–24,30,31,43} was in fact overestimated. Therefore that analysis should be characterized as highly conservative.

To compare experiment with theory, one should also take into account the surface roughness. The roughness profiles on both surfaces of sphere and plate were investigated using an AFM. The root-mean-square roughness on the sphere and the plate was found to be $\delta_s = 2.0$ nm and $\delta_p = 1.8$ nm, respectively. We have averaged the computed gradients of the Casimir force (11) to calculate the force gradient between rough surfaces F'_{theor} (the method

of geometrical averaging^{3,35}). At separations considered in this experiment ($a \geq 235$ nm) the same results for F'_{theor} were obtained after the multiplication of Eq. (11) by the factor

$$\eta_R(a) = 1 + 10 \frac{\delta_s^2 + \delta_p^2}{a^2} + 105 \frac{(\delta_s^2 + \delta_p^2)^2}{a^4}, \quad (13)$$

i.e., using the multiplicative approach.^{3,35} This is explained by the fact that at such large separations and small roughness the influence of roughness on force gradients is very small. Thus, at the shortest separation $a = 235$ nm it contributes only 0.13% of the force gradient. The role of surface roughness further decreases with the increase of separation between the surfaces.

The comparison of the experimental data obtained with applied compensating voltage to the plate (Sec. IVA) with theory is shown in Fig. 12(a-d) over different separation regions. The experimental data are shown as crosses with the total experimental errors determined at a 67% confidence level. The exact theoretical results for F'_{theor} computed using the Drude model approach, as explained above, are shown by the black bands. The widths of these bands are determined by the error in the sphere radius and by the errors in the optical data of Au defined by the number of significant figures in the tables.⁶⁷ Recall that the use of alternative optical data⁷⁰ and respective values of $\omega_p \leq 8$ eV makes F'_{theor} much smaller and, thus, further increases discrepancy between experiment and theory. Furthermore, for such optical data a significant disagreement was found⁶⁸ between the dielectric permittivities obtained by the extrapolation using the Drude model and by the weighted Kramers-Kronig relations. By the grey bands in Fig. 12(a-d) we present the theoretical results for F'_{theor} as a function of separation found using the plasma model approach. They are computed by Eq. (9) multiplied by the factor (13) to take into account the surface roughness. The error arising from the use of the PFA is included in the widths of grey bands. These widths take into account that the correction due to inaccuracy of the PFA is between $-0.564a/R$ and zero (it was shown⁶⁴⁻⁶⁶ that for real metals at $T \neq 0$ the magnitude of the main correction to the PFA is smaller than for ideal metal).

From Fig. 12(a-d) it can be seen that theoretical predictions obtained using the plasma model approach are in excellent agreement with the data over the entire range of separations. As to the predictions of the Drude model approach, they are excluded by the measurement data over the wide separation region from 235 to 420 nm. At larger separation distances the vertical arms of the crosses only touch the theoretical band predicted by the Drude model

approach, whereas the centers of crosses are still far away from the theoretical predictions. Thus, the experimental data obtained with applied compensating voltage are consistent with the predictions of the plasma model approach and exclude the Drude model approach. This is in accordance with the results obtained previously using another experimental technique.²¹⁻²⁴

We now compare with theory the experimental gradients of the Casimir force measured with different applied voltages to the plate (see Sec. IVB). In this case the results of the comparison are shown in Fig. 13(a-d), where the experimental data are indicated as crosses. As in Fig. 12, the black bands are computed using the exact theory in the framework of the Drude model approach. The grey bands are computed using the PFA and the plasma model approach. The error in the plasma model approach is included in the widths of grey bands. The results of the comparison between experiment and theory are the same as in Fig. 12. The plasma model approach is found in excellent agreement with the experimental data over the entire measurement range (shown in Fig. 13 and also at larger separations). The Drude model approach is excluded by the data over the separation region from 235 to 420 nm at a 67% confidence level. At larger separations the vertical arms of the crosses only touch the black theoretical bands whereas the centers of the crosses continue to belong to the grey bands.

We emphasize that the use of the exact theory in computations of the black bands (the Drude model approach) does not influence the obtained conclusions. Although the correction to the PFA result in Eq. (11) is negative and slightly increases the deviation between the data and the black bands in Figs. 12 and 13, the separation range where the Drude model approach is excluded (from 235 to 420 nm) remains the same irrespective of whether the exact theory or the PFA is used.

VI. NONLINEAR EFFECTS IN DYNAMIC TECHNIQUE

As was noted in Sec. II, in the dynamic technique, when the cantilever is oscillating, the separation distance between the sphere and the plate is varied harmonically in time

$$a(t) = a + A_z \cos \omega_r t, \quad (14)$$

where ω_r is the resonant frequency of the cantilever under the influence of the Casimir force and A_z is the oscillation amplitude which was chosen to be less than 10 nm. It was supposed

that under this condition at separations under consideration our oscillation system belongs to the linear regime where the shift of the natural frequency is given by Eq. (2). Here, we derive the analytic expression for the frequency shift in the nonlinear regime of an oscillator and determine the application region of Eq. (2).

The expressions for the shift of frequency of a nonlinear oscillator under the influence of the Casimir (Casimir-Polder) force were found perturbatively for the micromachined oscillator^{4,5} and exactly for the Bose-Einstein condensate cloud above a plate.⁷¹ The techniques involving shifts of the resonant frequency under the influence of an external force was discussed for the purpose of precise force measurements using different setups.^{49,72} The exact expression⁷¹ adapted to the case of an AFM with attached sphere in the nonlinear regime is given by

$$\omega_r^2 - \omega_0^2 = -\frac{\omega_r \omega_0^2}{\pi k A_z} \int_0^{2\pi/\omega_r} dt \cos(\omega_r t) F[a + A_z \cos(\omega_r t), T], \quad (15)$$

where F is the Casimir force acting between the sphere and the plate. Note that a similar equation was used⁷³ to investigate the nonlinear regime for a micromachined oscillator with attached cylinder interacting with a plate. Here we consider the measurement scheme with the applied compensating voltage when only the Casimir force causes the frequency shift of the oscillator. As was discussed in Sec. V, under the condition $a \ll R$ one can put with sufficient precision

$$F(z, T) = F_{\text{PFA}}(z, T) = k_B T R \sum_{l=0}^{\infty}{}' \int_0^{\infty} k_{\perp} dk_{\perp} \times \sum_{\alpha} \ln(1 - r_{\alpha}^2 e^{-2q_{\alpha} z}). \quad (16)$$

Substituting Eq. (16) into Eq. (15) and expanding the logarithms into power series, one obtains

$$\omega_r^2 - \omega_0^2 = \frac{\omega_r \omega_0^2}{\pi k A_z} k_B T R \int_0^{2\pi/\omega_r} dt \cos(\omega_r t) \times \sum_{l=0}^{\infty}{}' \int_0^{\infty} k_{\perp} dk_{\perp} \sum_{n=1}^{\infty} \frac{r_{\text{TM}}^{2n} + r_{\text{TE}}^{2n}}{n} e^{-2q_l n [a + A_z \cos(\omega_r t)]}. \quad (17)$$

Changing the order of summations and integrations and introducing the new variable $x =$

$\omega_r t$, we arrive at

$$\begin{aligned} \omega_r^2 - \omega_0^2 &= \frac{\omega_0^2}{\pi k A_z} k_B T R \sum_{l=0}^{\infty}{}' \sum_{n=1}^{\infty} \frac{1}{n} \int_0^{\infty} k_{\perp} dk_{\perp} \\ &\times (r_{\text{TM}}^{2n} + r_{\text{TE}}^{2n}) e^{-2naq_l} \int_0^{2\pi} dx \cos x e^{-2nq_l A_z \cos x}. \end{aligned} \quad (18)$$

The latter integral can be calculated explicitly⁷⁴

$$\int_0^{2\pi} dx \cos x e^{-2nq_l A_z \cos x} = -2\pi I_1(2nq_l A_z), \quad (19)$$

where $I_n(z)$ is the Bessel function of imaginary argument.

Taking into account that the frequency shift under the influence of the Casimir force is small in comparison with the resonant frequency, it holds

$$\omega_r^2 - \omega_0^2 = (\omega_r - \omega_0)(\omega_r + \omega_0) \approx 2\omega_0(\omega_r - \omega_0). \quad (20)$$

Then Eq. (18) can be rewritten as

$$\begin{aligned} \omega_r - \omega_0 &= -\frac{\omega_0}{k A_z} k_B T R \sum_{l=0}^{\infty}{}' \sum_{n=1}^{\infty} \frac{1}{n} \int_0^{\infty} k_{\perp} dk_{\perp} \\ &\times (r_{\text{TM}}^{2n} + r_{\text{TE}}^{2n}) e^{-2naq_l} I_1(2nq_l A_z). \end{aligned} \quad (21)$$

In terms of dimensionless variable $y = 2aq_l$ Eq. (21) takes the form

$$\begin{aligned} \omega_r - \omega_0 &= -\frac{\omega_0}{4a^2 k A_z} k_B T R \sum_{l=0}^{\infty}{}' \sum_{n=1}^{\infty} \frac{1}{n} \\ &\times \int_{\zeta_l}^{\infty} y dy (r_{\text{TM}}^{2n} + r_{\text{TE}}^{2n}) e^{-ny} I_1\left(\frac{A_z}{a} ny\right), \end{aligned} \quad (22)$$

where $\zeta_l = 2a\xi_l/c$ is the dimensionless Matsubara frequency. This is the final analytic expression for the frequency shift of a cantilever in the nonlinear regime.

Let us compare Eq. (22) with Eq. (2) and determine the application region of the latter. For this purpose we represent the Bessel function as power series⁷⁴

$$I_1(z) = \frac{z}{2} + \frac{z^3}{16} + O(z^5) \quad (23)$$

and substitute the first two terms into Eq. (22):

$$\begin{aligned} \omega_r - \omega_0 &= -\frac{\omega_0}{8a^3 k} k_B T R \sum_{l=0}^{\infty}{}' \sum_{n=1}^{\infty} \int_{\zeta_l}^{\infty} y^2 dy \\ &\times (r_{\text{TM}}^{2n} + r_{\text{TE}}^{2n}) e^{-ny} \\ &- \frac{\omega_0 A_z^2}{64a^5 k} k_B T R \sum_{l=0}^{\infty}{}' \sum_{n=1}^{\infty} n^2 \int_{\zeta_l}^{\infty} y^4 dy (r_{\text{TM}}^{2n} + r_{\text{TE}}^{2n}) e^{-ny}. \end{aligned} \quad (24)$$

The sum in n in the first term on the right-hand side of Eq. (24) is calculated as

$$\sum_{n=1}^{\infty} (r_{\text{TM}}^2 + r_{\text{TE}}^2) e^{-ny} = \frac{r_{\text{TM}}^2}{e^y - r_{\text{TM}}^2} + \frac{r_{\text{TE}}^2}{e^y - r_{\text{TE}}^2}. \quad (25)$$

By comparing Eq. (24) and (9) with account of Eq. (25) and the connection between dimensional and dimensionless variables, we arrive at

$$\begin{aligned} \omega_r - \omega_0 &= -\frac{\omega_0}{2k} \frac{\partial F_{\text{PFA}}(a, T)}{\partial a} - \frac{\omega_0 A_z^2}{64a^5 k} k_B T R \\ &\times \sum_{l=0}^{\infty} \sum_{n=1}^{\infty} n^2 \int_{\zeta_l}^{\infty} y^4 dy (r_{\text{TM}}^{2n} + r_{\text{TE}}^{2n}) e^{-ny}. \end{aligned} \quad (26)$$

Furthermore, taking into account that

$$\begin{aligned} \sum_{n=1}^{\infty} n^2 (r_{\text{TM}}^2 + r_{\text{TE}}^2) e^{-ny} &= r_{\text{TM}}^2 e^{-y} \frac{1 + r_{\text{TM}}^2 e^{-y}}{(1 - r_{\text{TM}}^2 e^{-y})^3} \\ &+ r_{\text{TE}}^2 e^{-y} \frac{1 + r_{\text{TE}}^2 e^{-y}}{(1 - r_{\text{TE}}^2 e^{-y})^3}, \end{aligned} \quad (27)$$

we rewrite Eq. (26) in the form

$$\begin{aligned} \omega_r - \omega_0 &= -\frac{\omega_0}{2k} \frac{\partial F_{\text{PFA}}(a, T)}{\partial a} - \frac{\omega_0 A_z^2}{64a^5 k} k_B T R \\ &\times \sum_{l=0}^{\infty} \int_{\zeta_l}^{\infty} y^4 dy \left[r_{\text{TM}}^2 e^{-y} \frac{1 + r_{\text{TM}}^2 e^{-y}}{(1 - r_{\text{TM}}^2 e^{-y})^3} \right. \\ &\left. + r_{\text{TE}}^2 e^{-y} \frac{1 + r_{\text{TE}}^2 e^{-y}}{(1 - r_{\text{TE}}^2 e^{-y})^3} \right]. \end{aligned} \quad (28)$$

Here, the first term on the right-hand side coincides with the right-hand side of Eq. (2) (the linear regime), whereas the second term describes nonlinear corrections (note that the total force now coincides with the Casimir force).

One can restrict oneself to the linear regime if the magnitude of the second term is much smaller than that of the first. Keeping in mind that the force gradient is connected with the pressure by means of Eq. (7), this condition can be written as

$$\begin{aligned} |P(a, T)| &\gg \frac{k_B T A_z^2}{64a^5} \sum_{l=0}^{\infty} \int_{\zeta_l}^{\infty} y^4 dy \\ &\times \sum_{\alpha} \left[r_{\text{TM}}^2 e^{-y} \frac{1 + r_{\text{TM}}^2 e^{-y}}{(1 - r_{\text{TM}}^2 e^{-y})^3} + r_{\text{TE}}^2 e^{-y} \frac{1 + r_{\text{TE}}^2 e^{-y}}{(1 - r_{\text{TE}}^2 e^{-y})^3} \right]. \end{aligned} \quad (29)$$

We have calculated the quantity in the right-hand side of Eq. (29) for the parameters of our experimental setup under the condition that this quantity does not exceed 1% of the

magnitude of the Casimir pressure. The obtained maximum allowed oscillation amplitudes of the cantilever are shown in Fig. 14 as a function of separation by the solid and dashed lines for the plasma and Drude model approaches, respectively. The allowed regions in the plane (a, A_z) , where the contribution of nonlinear effects is less than 1%, lie beneath the lines. As an example, at separations 100, 235, 300 and 500 nm the oscillation amplitude should not exceed 7.07, 16.1, 20.2, and 32.8 nm if computations are performed using the Drude model approach. If computations are performed using the plasma model approach only slightly different maximum amplitudes are allowed. They are equal to 7.11, 16.2, 20.5, and 33.4 nm at the same respective separations.

Note that the use of full Eqs. (22) and (28) opens opportunities for performing measurements in the nonlinear regime. In this case the immediately measured quantity would be the frequency shift to be compared with theoretical computations using Eqs. (22) or (28) with different dielectric properties of boundary surfaces.

VII. CONCLUSIONS AND DISCUSSION

In the foregoing we have presented the results of precise measurements of the gradient of the Casimir force between an Au-coated sphere and a plate by means of an AFM operated in the dynamic regime. From several modifications of dynamic measurements the most sensitive frequency shift technique has been employed which has never been used before in experiments on the Casimir force using an AFM. This was connected with creation of significantly different setup adapted for dynamic measurements, use of higher vacuum and hollow glass microspheres of smaller radius.

Special attention was devoted to electrostatic calibrations of the setup, i.e., to a problem which created much discussion in previous literature. We have addressed in much detail both the problem of electrostatic patches and contaminants on the surface and the problem of dependence of the calibration parameters on separation between the test bodies. It is well known that many different models of patches were discussed in the literature leading to varying predictions of additional electrostatic forces from large⁵⁸ to negligibly small.⁷⁵ To address this problem, we performed numerical simulation of the electrostatic force due to the patch potentials and have shown that for both relatively small and large patches the residual potential between the sphere and the plate would be separation-dependent for

patch sizes of order or larger than the separation. This adds importance to the second problem, i.e., to the separation-dependence of the calibration parameters. Experimental investigation of this problem demonstrated that the calibration parameters are constant if the corrections to mechanical drift are introduced. Our measurement data for electric forces unequivocally exclude the predicted⁵⁸ large electrostatic force from the polycrystal structure of Au coatings. On the other hand, the observed independence of the residual potential difference on separation rejects the hypothesis⁵⁸ of large contaminants on the surface, which could decrease significantly the enormously large effect of a polycrystal structure, but, as follows from our simulations, lead to the separation-dependent residual potential. These findings are in line with the fact that the surfaces of the Au-coated sphere and the plate in our experiment have been subjected to a multistep cleaning procedure and would be unlikely to have large contaminants. Thus, our conclusion is that the experimental data are in favor of the model of patches proposed previously.⁷⁵

It should be stressed that the mean gradient of the Casimir force as a function of separation has been measured in our experiment in two independent ways (with applied compensating voltage and with applied different voltages to the plate with subsequent subtraction of electric forces). The obtained results were found in excellent agreement in the limits of total experimental errors. The latter were determined as combinations of random and systematic errors at a 67% confidence level. The mean measured gradients of the Casimir force were converted into the pressure between two parallel plates and compared with respective results measured in the most precise experiment performed by means of micromachined oscillator.^{23,24} The mean Casimir pressures determined in both experiments were found in excellent agreement over the entire measurement range.

The mean measured gradients of the Casimir force were compared with theoretical predictions of the Lifshitz theory with no fitting parameters. In so doing two theoretical approaches proposed in the literature were used based on the Drude and plasma models of dielectric permittivity. The contribution of surface roughness was calculated to be less than 0.13% of the force gradients. The measured data were shown to be consistent with theoretical results obtained using the generalized plasma-like model over the entire measurement range. Theoretical predictions computed using the Drude model approach were excluded by the data over the separation region from 235 to 420 nm at a 67% confidence level with measurements at every nanometer. The nonlinear regime of our oscillator was investigated, and the linear-

ity in the region of used experimental parameters was confirmed. It is pertinent to note that one experiment alone performed at a 67% confidence level would be not enough to falsify application in Casimir physics of a well tested and commonly used theoretical model. In this regard our experiment should be considered as an additional independent argument to more precise experiments (up to 99.9% confidence level) performed using another experimental technique.^{3,22-24}

The main result on the exclusion of the Drude model by the data deserves special discussion. It is common knowledge that response of metallic materials to real electromagnetic fields is correctly described by the Drude model, whereas the plasma model is only an approximation valid in the region of sufficiently high frequencies. Experiments using a micromachined oscillator²¹⁻²⁴ demonstrated that in the Lifshitz theory not the Drude but the plasma model is supported by the data. Thereafter many attempts were undertaken to rule out this conclusion. This is the reason why one more experiment, using an alternative laboratory setup, is highly desirable. In our experiment, using a dynamic AFM in a frequency modulation technique, we confirmed the results of previous measurements performed by means of a micromachined oscillator. We also addressed the problem of patch potentials, independence of the calibration parameters on separation and applicability of the linear regime of the dynamic AFM. In addition, an independent comparison between experiment and theory beyond the PFA has been made with no fitting parameters. Nevertheless the Drude model approach was again excluded by the data. One can conclude that the exclusion of this approach to a theoretical description of the Casimir interaction between metallic surfaces received a more complete experimental confirmation. Keeping in mind similar experiments with semiconductor and dielectric test bodies discussed in Sec. I, a thorough analysis of all the assumptions in the basics of the Lifshitz theory seems pertinent.

Acknowledgments

The authors are grateful to G. Bimonte for providing the numerical values of a correction beyond the PFA from Fig. 2 of Ref.⁶⁴. This work was supported by the NSF Grant No. PHY0970161 (C.-C.C., G.L.K., V.M.M., U.M.), DOE Grant No. DEF010204ER46131 (equipment, G.L.K., V.M.M., U.M.) and DARPA Grant under Contract No. S-000354 (A.B., R.C.-G., U.M.). G.L.K. and V.M.M. were also partially supported by the DFG grant BO

-
- ¹ H. B. G. Casimir, Proc. K. Ned. Akad. Wet. B **51**, 793 (1948).
- ² M. Bordag, U. Mohideen, and V. M. Mostepanenko, Phys. Rep. **353**, 1 (2001).
- ³ G. L. Klimchitskaya, U. Mohideen, and V. M. Mostepanenko, Rev. Mod. Phys. **81**, 1827 (2009).
- ⁴ H. B. Chan, V. A. Aksyuk, R. N. Kleiman, D. J. Bishop, and F. Capasso, Science **291**, 1941 (2001).
- ⁵ H. B. Chan, V. A. Aksyuk, R. N. Kleiman, D. J. Bishop, and F. Capasso, Phys. Rev. Lett. **87**, 211801 (2001).
- ⁶ E. Buks and M. L. Roukes, Phys. Rev. B **63**, 033402 (2001).
- ⁷ V. M. Mostepanenko and I. Yu. Sokolov, Phys. Lett. A **125**, 405 (1987).
- ⁸ V. M. Mostepanenko and I. Yu. Sokolov, Phys. Lett. A **132**, 313 (1988).
- ⁹ R. Onofrio, New J. Phys. **8**, 237 (2006).
- ¹⁰ V. B. Bezerra, G. L. Klimchitskaya, V. M. Mostepanenko, and C. Romero, Phys. Rev. D **81**, 055003 (2010).
- ¹¹ V. B. Bezerra, G. L. Klimchitskaya, V. M. Mostepanenko, and C. Romero, Phys. Rev. D **83**, 075004 (2011).
- ¹² A. O. Sushkov, W. J. Kim, D. A. R. Dalvit, and S. K. Lamoreaux, Phys. Rev. Lett. **107**, 171101 (2011).
- ¹³ E. M. Lifshitz, Zh. Eksp. Teor. Fiz. **29**, 94 (1955) [Sov. Phys. JETP **2**, 73 (1956)].
- ¹⁴ E. M. Lifshitz and L. P. Pitaevskii, *Statistical Physics*, Part II (Pergamon, Oxford, 1980).
- ¹⁵ M. Boström and B. E. Sernelius, Phys. Rev. Lett. **84**, 4757 (2000).
- ¹⁶ C. Genet, A. Lambrecht, and S. Reynaud, Phys. Rev. A **62**, 012110 (2000).
- ¹⁷ M. Bordag, B. Geyer, G. L. Klimchitskaya, and V. M. Mostepanenko, Phys. Rev. Lett. **85**, 503 (2000).
- ¹⁸ T. Emig, R. L. Jaffe, M. Kardar, and A. Scardicchio, Phys. Rev. Lett. **96**, 080403 (2006).
- ¹⁹ T. Emig, N. Graham, R. L. Jaffe, and M. Kardar, Phys. Rev. Lett. **99**, 017403 (2007).
- ²⁰ O. Kenneth and I. Klich, Phys. Rev. B **78**, 014103 (2008).
- ²¹ R. S. Decca, E. Fischbach, G. L. Klimchitskaya, D. E. Krause, D. López, and V. M. Mostepanenko, Phys. Rev. D **68**, 116003 (2003).

- ²² R. S. Decca, D. López, E. Fischbach, G. L. Klimchitskaya, D. E. Krause, and V. M. Mostepanenko, *Ann. Phys. (N.Y.)* **318**, 37 (2005).
- ²³ R. S. Decca, D. López, E. Fischbach, G. L. Klimchitskaya, D. E. Krause, and V. M. Mostepanenko, *Phys. Rev. D* **75**, 077101 (2007).
- ²⁴ R. S. Decca, D. López, E. Fischbach, G. L. Klimchitskaya, D. E. Krause, and V. M. Mostepanenko, *Eur. Phys. J. C* **51**, 963 (2007).
- ²⁵ G. Bressi, G. Carugno, R. Onofrio, and G. Ruoso, *Phys. Rev. Lett.* **88**, 041804 (2002).
- ²⁶ V. B. Bezerra, G. L. Klimchitskaya, V. M. Mostepanenko, and C. Romero, *Phys. Rev. A* **69**, 022119 (2004).
- ²⁷ K. A. Milton, *J. Phys. A: Math. Gen.* **37**, R209 (2004).
- ²⁸ I. Brevik, J. B. Aarseth, J. S. Høye, and K. A. Milton, *Phys. Rev. E* **71**, 056101 (2005).
- ²⁹ G. L. Klimchitskaya and V. M. Mostepanenko, *Int. J. Mod. Phys. A* **25**, 2302 (2010).
- ³⁰ F. Chen, G. L. Klimchitskaya, V. M. Mostepanenko, and U. Mohideen, *Optics Express* **15**, 4823 (2007).
- ³¹ F. Chen, G. L. Klimchitskaya, V. M. Mostepanenko, and U. Mohideen, *Phys. Rev. B* **76**, 035338 (2007).
- ³² J. M. Obrecht, R. J. Wild, M. Antezza, L. P. Pitaevskii, S. Stringari, and E. A. Cornell, *Phys. Rev. Lett.* **98**, 063201 (2007).
- ³³ G. L. Klimchitskaya and V. M. Mostepanenko, *J. Phys. A: Math. Theor.* **41**, 312002(F) (2008).
- ³⁴ B. Geyer, G. L. Klimchitskaya, and V. M. Mostepanenko, *Phys. Rev. D* **72**, 085009 (2005).
- ³⁵ M. Bordag, G. L. Klimchitskaya, U. Mohideen, and V. M. Mostepanenko, *Advances in the Casimir Effect* (Oxford University Press, Oxford, 2009).
- ³⁶ A. W. Rodriguez, F. Capasso, and S. G. Johnson, *Nature Photon.* **5**, 211 (2011).
- ³⁷ G. L. Klimchitskaya, U. Mohideen, and V. M. Mostepanenko, *Int. J. Mod. Phys. B* **25**, 171 (2011).
- ³⁸ A. O. Sushkov, W. J. Kim, D. A. R. Dalvit, and S. K. Lamoreaux, *Nature Phys.* **7**, 230 (2011).
- ³⁹ S. K. Lamoreaux, *Phys. Rev. Lett.* **78**, 5 (1997).
- ⁴⁰ M. Masuda and M. Sasaki, *Phys. Rev. Lett.* **102**, 171101 (2009).
- ⁴¹ G. L. Klimchitskaya, M. Bordag, E. Fischbach, D. E. Krause, and V. M. Mostepanenko, *Int. J. Mod. Phys. A* **26**, 3918 (2011).
- ⁴² V. B. Bezerra, G. L. Klimchitskaya, U. Mohideen, V. M. Mostepanenko, and C. Romero, *Phys.*

- Rev. B **83**, 075417 (2011).
- ⁴³ C.-C. Chang, A. A. Banishev, G. L. Klimchitskaya, V. M. Mostepanenko, and U. Mohideen, Phys. Rev. Lett. **107**, 090403 (2011).
- ⁴⁴ A. A. Banishev, C.-C. Chang, R. Castillo-Garza, G. L. Klimchitskaya, V. M. Mostepanenko, and U. Mohideen, Phys. Rev. B **85**, 045436 (2012).
- ⁴⁵ B. W. Harris, F. Chen, and U. Mohideen, Phys. Rev. A **62**, 052109 (2000).
- ⁴⁶ G. Jourdan, A. Lambrecht, F. Comin, and J. Chevrier, Europhys. Lett. **85**, 31001 (2009).
- ⁴⁷ J. Laurent, H. Sellier, A. Mosset, S. Huant, and J. Chevrier, Phys. Rev. B **85**, 035426 (2012).
- ⁴⁸ S. de Man, K. Heeck, R. J. Wijngaarden, and D. Iannuzzi, Phys. Rev. Lett. **103**, 040402 (2009).
- ⁴⁹ F. J. Giessibl, Rev. Mod. Phys. **75**, 949 (2003).
- ⁵⁰ H.-C. Chiu, C.-C. Chang, R. Castillo-Garza, F. Chen, and U. Mohideen, J. Phys. A **41**, 164022 (2008).
- ⁵¹ F. Chen and U. Mohideen, Rev. Sci. Instrum. **72**, 3100 (2001).
- ⁵² W. R. Smythe, *Electrostatics and Electrodynamics* (McGraw-Hill, New York, 1950).
- ⁵³ F. Chen, U. Mohideen, G. L. Klimchitskaya, and V. M. Mostepanenko, Phys. Rev. A **74**, 022103 (2006).
- ⁵⁴ W. J. Kim, M. Brown-Hayes, D. A. R. Dalvit, J. H. Brownell, and R. Onofrio, Phys. Rev. A **78**, 020101(R) (2008).
- ⁵⁵ R. S. Decca, E. Fischbach, G. L. Klimchitskaya, D. E. Krause, D. López, U. Mohideen, and V. M. Mostepanenko, Phys. Rev. A **79**, 026101 (2009).
- ⁵⁶ W. J. Kim, M. Brown-Hayes, D. A. R. Dalvit, J. H. Brownell, and R. Onofrio, Phys. Rev. A **79**, 026102 (2009).
- ⁵⁷ R. S. Decca, E. Fischbach, G. L. Klimchitskaya, D. E. Krause, D. López, U. Mohideen, and V. M. Mostepanenko, Int. J. Mod. Phys. A **26**, 3930 (2011).
- ⁵⁸ R. O. Behunin, F. Intravaia, D. A. R. Dalvit, P. A. Maia Neto, and S. Reynaud, Phys. Rev. A **85**, 012504 (2012).
- ⁵⁹ N. Gaillard, M. Gros-Jean, D. Mariolle, F. Bertin, and A. Bsiesy, Appl. Phys. Lett. **89**, 154101 (2006).
- ⁶⁰ F. Rossi and G. I. Opat, J. Phys. D **25**, 1349 (1992).
- ⁶¹ *CRC Handbook of Chemistry and Physics*, ed. C. R. Lide (CRC Press, Boca Raton, 2001).
- ⁶² Q. Wei, D. A. R. Dalvit, F. C. Lombardo, F. D. Mazzitelli, and R. Onofrio, Phys. Rev. A **81**,

- 052115 (2010).
- ⁶³ G. Bimonte, T. Emig, R. L. Jaffe, and M. Kardar, *Europhys. Lett.* **97**, 50001 (2012).
- ⁶⁴ G. Bimonte, T. Emig, and M. Kardar, *Appl. Phys. Lett.* **100**, 074110 (2012).
- ⁶⁵ A. Canaguier-Durand, P. A. Maia Neto, A. Lambrecht, and S. Reynaud, *Phys. Rev. Lett.* **104**, 040403 (2010).
- ⁶⁶ R. Zandi, T. Emig, and U. Mohideen, *Phys. Rev. B* **81**, 195423 (2010).
- ⁶⁷ *Handbook of Optical Constants of Solids*, ed. E. D. Palik (Academic, New York, 1985).
- ⁶⁸ G. Bimonte, *Phys. Rev. A* **83**, 042109 (2011).
- ⁶⁹ L. P. Teo, M. Bordag, and V. Nikolaev, *Phys. Rev. D* **84**, 125037 (2011).
- ⁷⁰ V. B. Svetovoy, P. J. van Zwol, G. Palasantzas, and J. Th. M. De Hosson, *Phys. Rev. B* **77**, 035439 (2008).
- ⁷¹ M. Antezza, L. P. Pitaevskii, and S. Stringari, *Phys. Rev. A* **70**, 053619 (2004).
- ⁷² G. Bressi, G. Carugno, A. Galvani, R. Onofrio, and G. Ruoso, *Class. Quant. Grav.* **17**, 2365 (2000).
- ⁷³ R. S. Decca, E. Fischbach, G. L. Klimchitskaya, D. E. Krause, D. López, and V. M. Mostepanenko, *Phys. Rev. A* **84**, 042502 (2011).
- ⁷⁴ I. S. Gradshteyn and I. M. Ryzhik, *Tables of Integrals, Series, and Products* (Academic, New York, 1980).
- ⁷⁵ C. C. Speake and C. Trenkel, *Phys. Rev. Lett.* **90**, 160403 (2003).

Figures

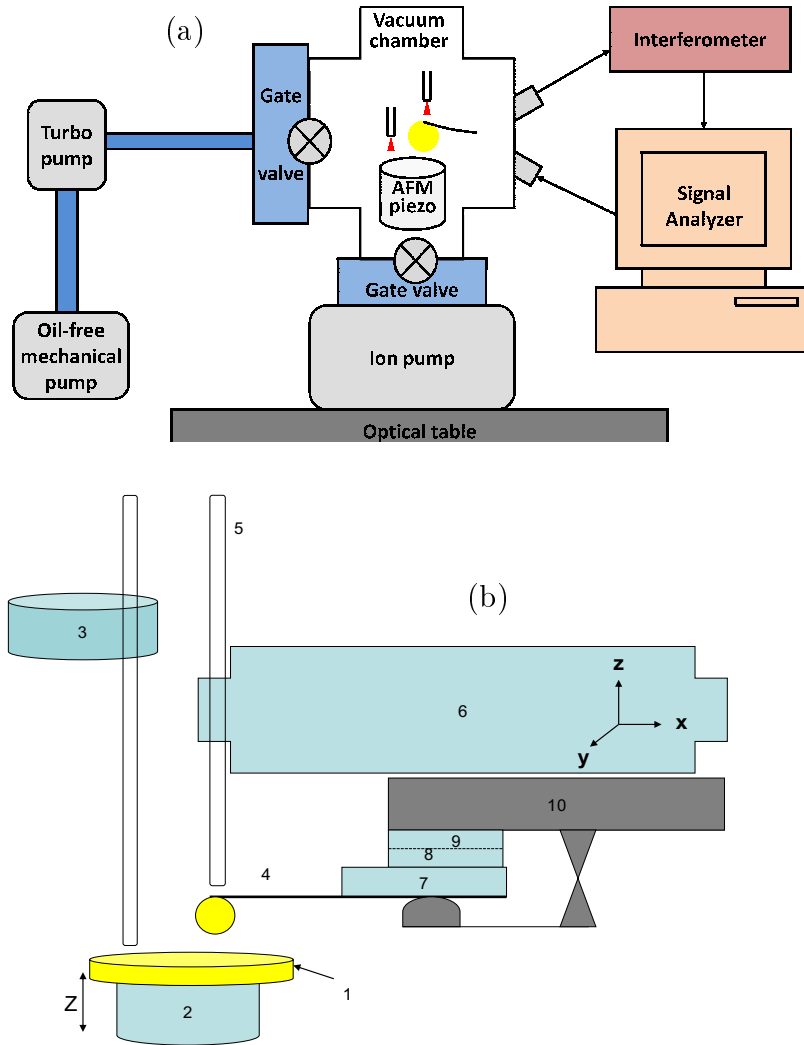


FIG. 1: (Color online) (a) Layout of the vacuum FM-AFM setup used in precision dynamic measurements of the gradient of the Casimir force. (b) Schematic of the force measurements microscope. (1) is a Au plate placed on the AFM piezo (2). (3) is the plate movement interferometer detection fiber. For monitoring the cantilever (4) oscillations the second interferometer was used, the detection fiber end is shown as (5). The end was fixed in the fiber holder (6), which was placed in the XYZ stage and can move in the XYZ direction for adjusting the signal from cantilever. The cantilever chip (7) was connected to two piezoelectric actuators (8 and 9) and clutched in the home-made cantilever holder (10) as shown in the picture.

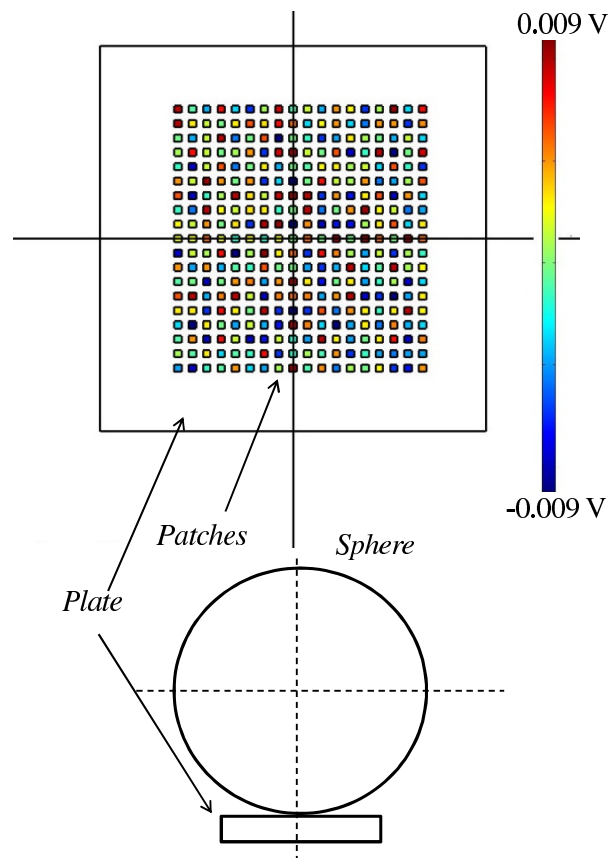


FIG. 2: (Color online) The sphere-plate configuration with patches which were put on the top of a plate.

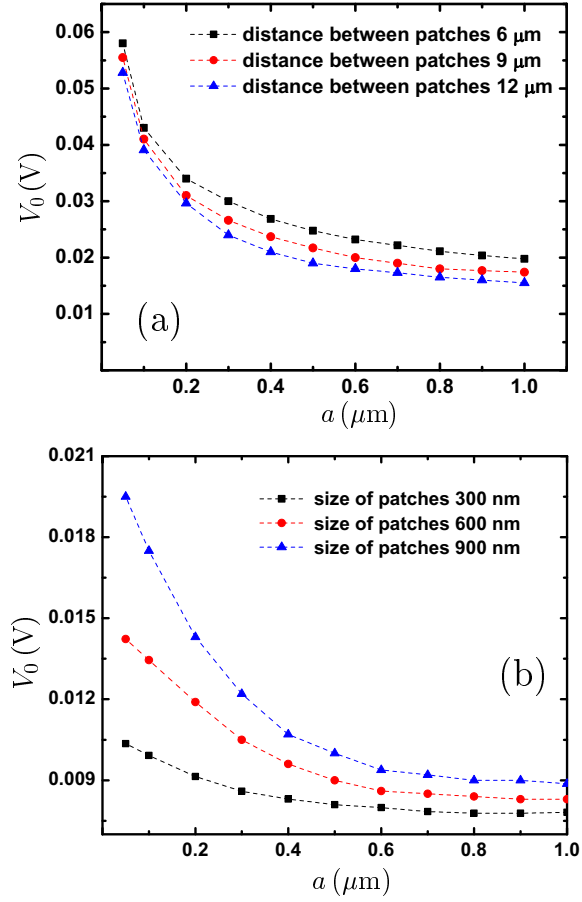


FIG. 3: (Color online) The residual potential difference between the sphere and the plate as a function of separation for (a) patches of fixed sizes $6 \times 6 \mu\text{m}^2$ with different distances between patches and (b) fixed distances between patches equal to 600 nm with different sizes of patches.

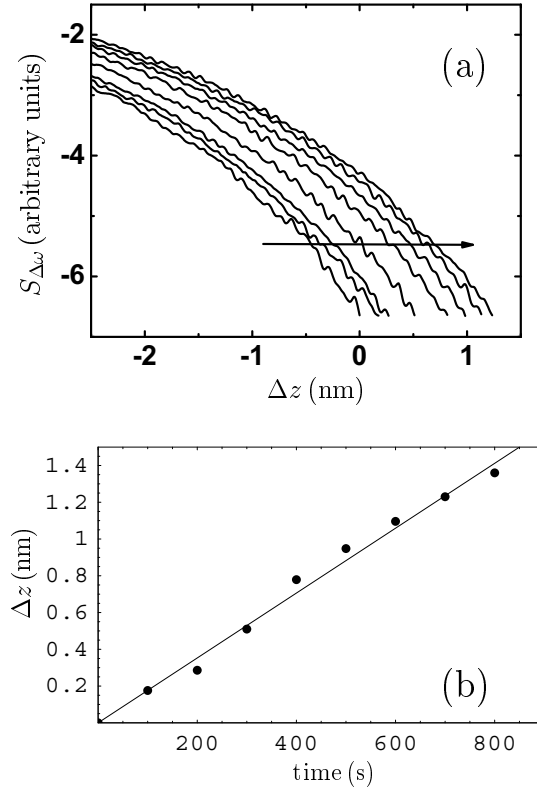


FIG. 4: (a) The drift in experimental curves for the frequency shift signal as a function of the change in sphere-plate separation for 8 repetitions of the same applied voltage to the plate. (b) The change in the plate position at one frequency shift signal value as a function of time.

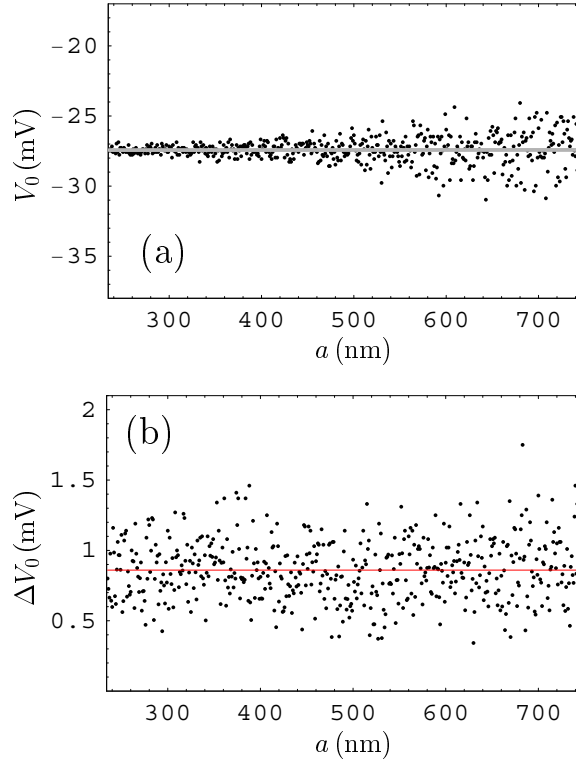


FIG. 5: (Color online) (a) The residual potential difference between Au-coated sphere and plate as a function of separation. (b) The systematic error of each individual V_0 , as determined from the fit, versus separation.

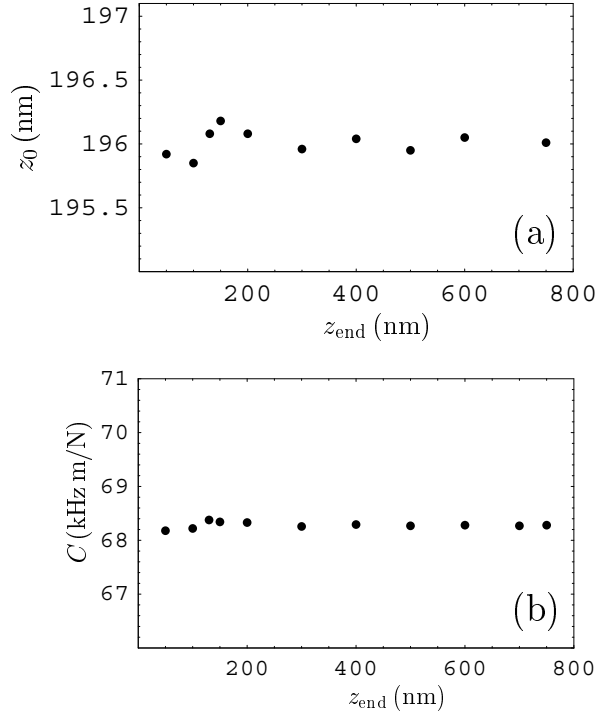


FIG. 6: The dependences of (a) the closest sphere-plate separation and (b) the coefficient C in Eq. (5) on the end point of the fit.

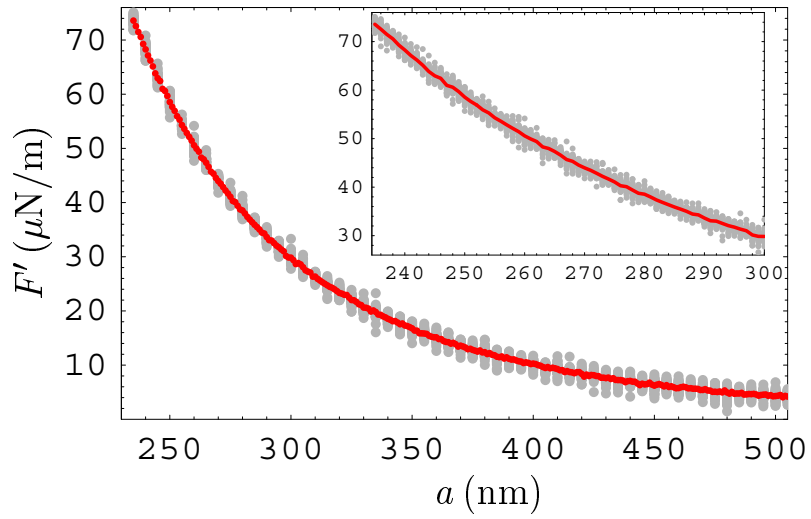


FIG. 7: (Color online) Mean measured gradients of the Casimir force as a function of separation are shown by solid lines. Grey dots indicate all 40 individual force gradients plotted with a step of 5 nm (1 nm in the inset).

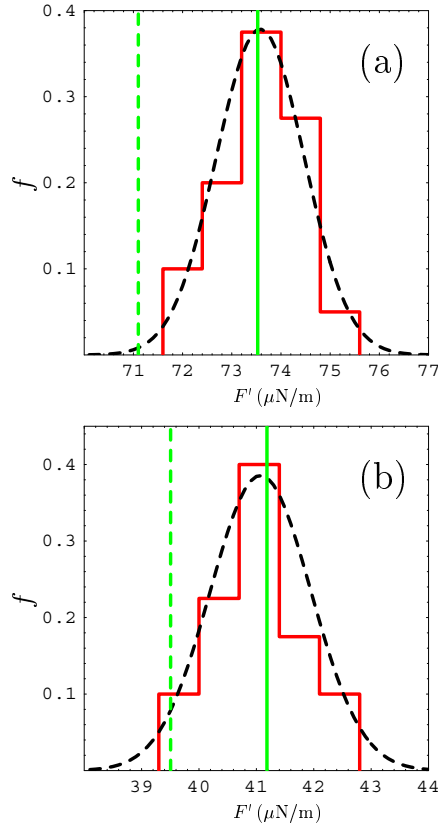


FIG. 8: (Color online) The histograms for the measured gradients of the Casimir force at separations (a) $a = 235$ nm and (b) $a = 275$ nm. f is the fraction of 40 data points having the force values in the bin indicated by the respective vertical lines of the histogram. The corresponding Gaussian distributions are shown by the dashed black lines. The solid and dashed vertical lines show the theoretical predictions from the plasma and Drude model approaches, respectively.

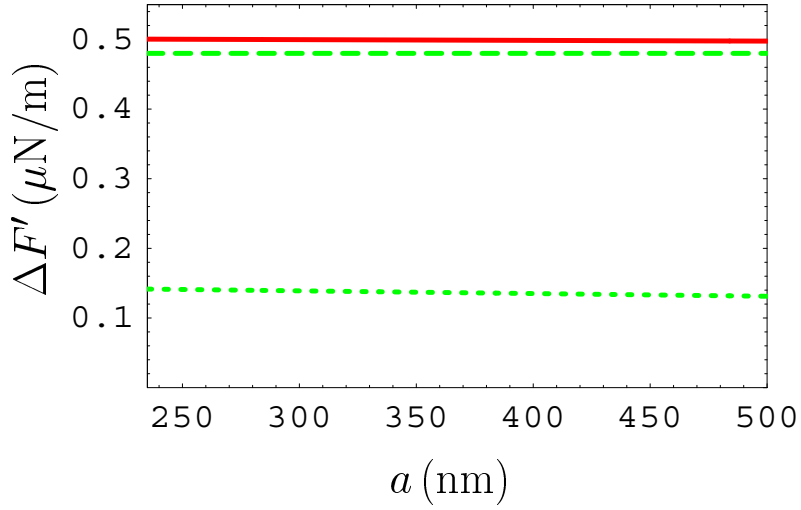


FIG. 9: (Color online) The random, systematic and total experimental errors in the measured gradients of the Casimir force determined at a 67% confidence level are shown by the short-dashed, long-dashed and solid lines, respectively. The measurement scheme with applied compensating voltage is used.

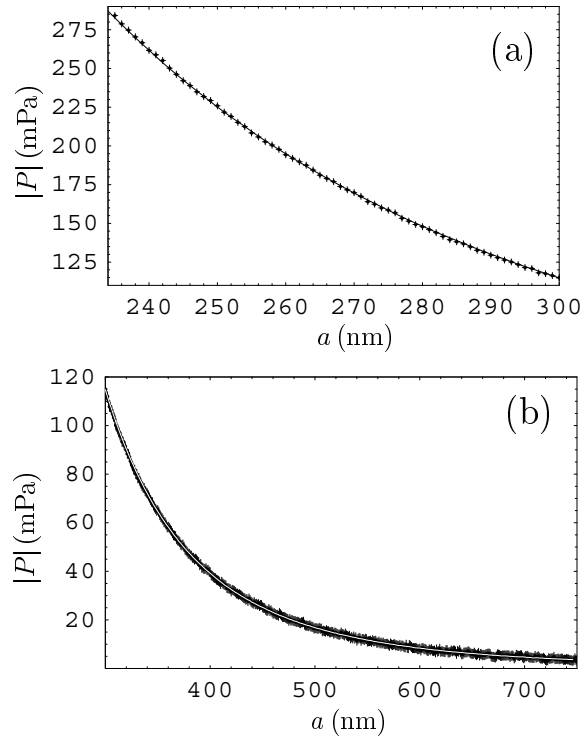


FIG. 10: Magnitudes of the mean Casimir pressure previously measured^{23,24} are shown by (a) black and (b) white lines as functions of separation. Magnitudes of the mean Casimir pressure measured here are indicated as crosses. The arms of the crosses are determined by errors in the measurement of separations and force gradients.

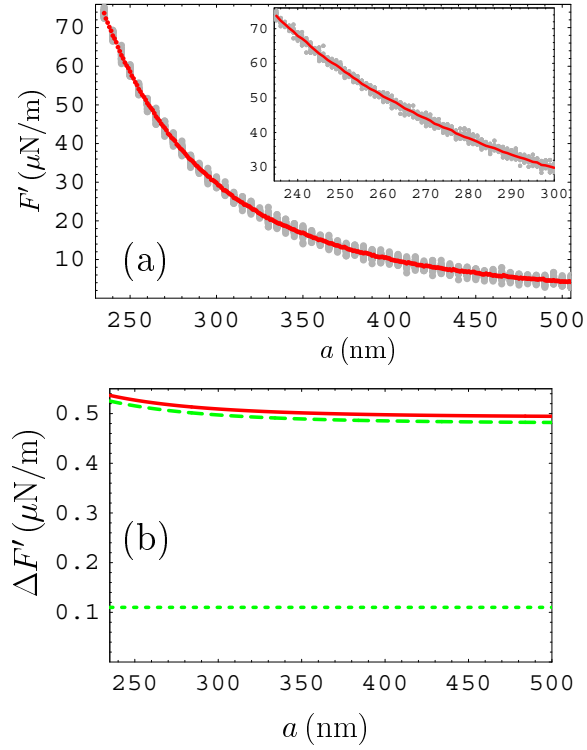


FIG. 11: (Color online) (a) Mean measured gradients of the Casimir force as a function of separation are shown by solid lines. Grey dots indicate all 40 individual force gradients plotted with the step of 5 nm (1 nm in the inset). (b) The random, systematic and total experimental errors in the measured gradient of the Casimir force determined at a 67% confidence level are shown by the short-dashed, long-dashed and solid lines, respectively. The measurement scheme with different applied voltages is used.

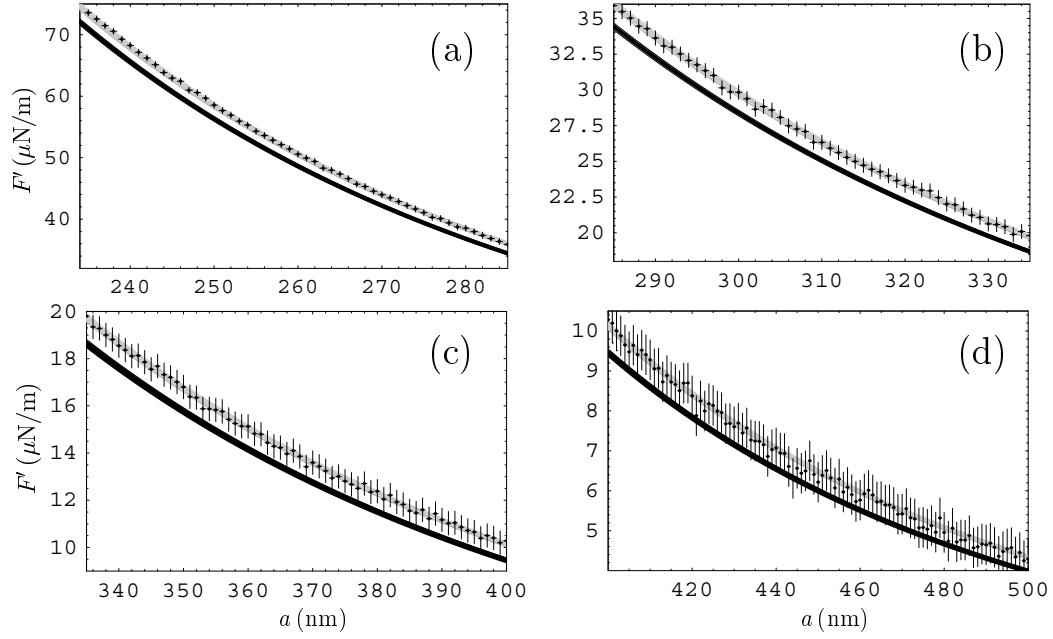


FIG. 12: Comparison between the experimental data for the gradient of the Casimir force (crosses plotted at a 67% confidence level) and theory (black and grey bands computed using the Drude and plasma model approaches, respectively) within different separation regions. The experimental data are obtained with the compensating voltage applied to the plate.

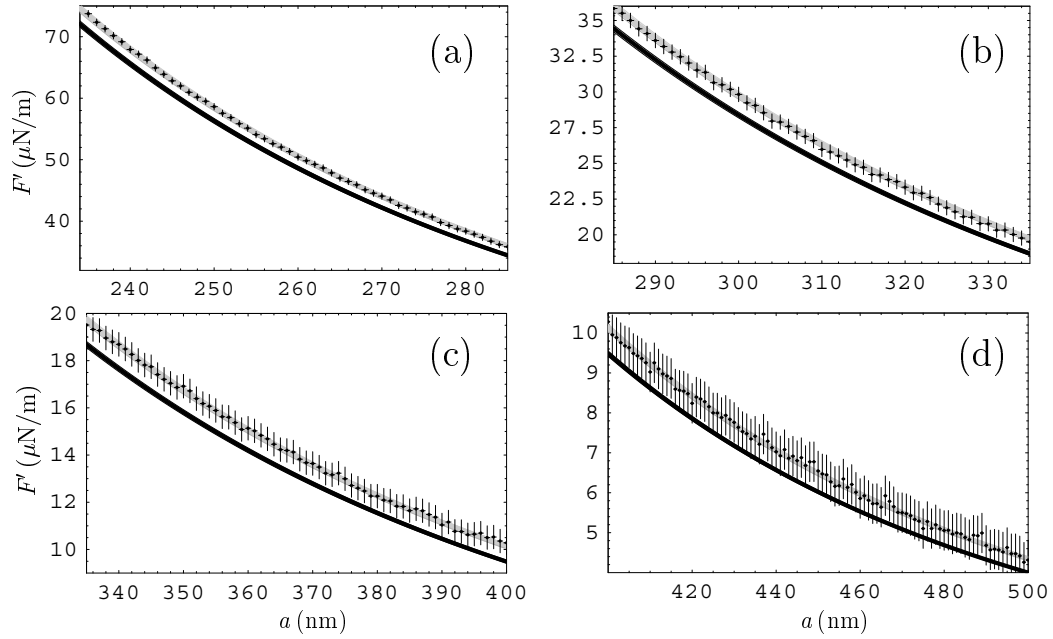


FIG. 13: Comparison between the experimental data for the gradient of the Casimir force (crosses plotted at a 67% confidence level) and theory (black and grey bands computed using the Drude and plasma model approaches, respectively) within different separation regions. The experimental data are obtained with different voltages applied to the plate.

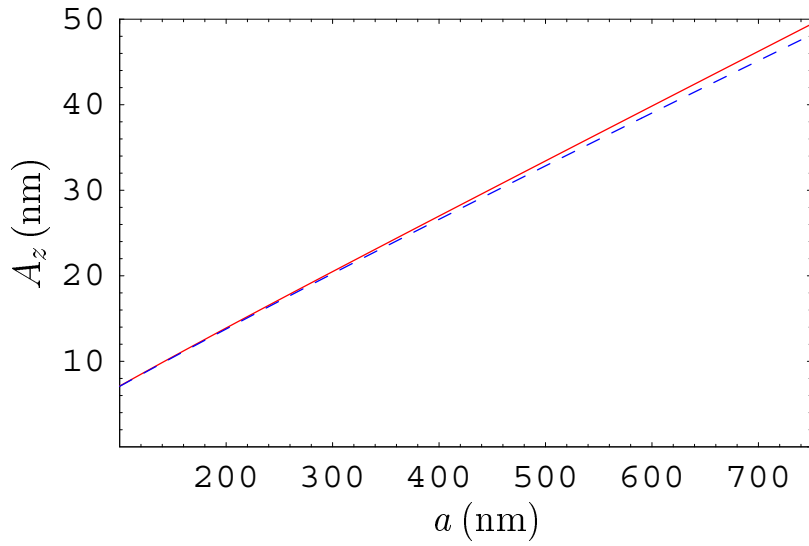


FIG. 14: Maximum allowed amplitudes of oscillations of the AFM cantilever in the linear regime as a function of separation are shown by the solid line (the plasma model approach) and by the dashed line (the Drude model approach). The allowed regions of (a, A_z) -plane lie beneath the lines.

Tables

TABLE I: The mean values of the gradients of the Casimir force together with their total experimental errors at different separations (column 1) measured in this work with applied compensating voltage (column 2) and with different applied voltages (column 3). Column 4 contains the mean gradients of the Casimir force and their total experimental errors obtained from the previously measured pressures.^{23,24}

a (nm)	Gradients of the Casimir force F' ($\mu\text{N}/\text{m}$)		
	measurements with applied V_0	measurements with different applied V_i	IUPUI
236	72.56 ± 0.50	72.35 ± 0.54	72.22 ± 0.34
240	68.27 ± 0.50	67.92 ± 0.53	67.91 ± 0.32
250	58.55 ± 0.50	58.62 ± 0.53	58.43 ± 0.29
260	50.57 ± 0.50	50.42 ± 0.52	50.57 ± 0.27
270	43.98 ± 0.50	44.08 ± 0.52	44.01 ± 0.25
280	38.55 ± 0.50	38.38 ± 0.51	38.47 ± 0.23
290	33.63 ± 0.50	33.60 ± 0.51	33.78 ± 0.22
300	29.83 ± 0.50	29.83 ± 0.51	29.79 ± 0.21
350	16.80 ± 0.50	16.92 ± 0.50	16.77 ± 0.18
400	10.28 ± 0.50	10.28 ± 0.50	10.17 ± 0.17
450	6.22 ± 0.50	6.54 ± 0.50	6.53 ± 0.16
500	4.29 ± 0.50	4.32 ± 0.49	4.36 ± 0.16
550	3.20 ± 0.50	2.87 ± 0.49	3.03 ± 0.16
600	2.51 ± 0.50	2.12 ± 0.49	2.18 ± 0.16
650	1.74 ± 0.50	1.56 ± 0.49	1.61 ± 0.16
700	1.16 ± 0.50	1.17 ± 0.49	1.23 ± 0.16
746	1.06 ± 0.50	0.82 ± 0.49	0.94 ± 0.16